EFFECT OF FLUID HYDRODYNAMICS ON CALCIUM SULPHATE "CASO4" DEPOSITION ON ALUMINIUM METAL SURFACE

BY

ABDULLAH ALI AL-MESFER

A Thesis Presented to the

DEANSHIP OF GRADUATE STUDIES

KING FAHD UNIVERSITY OF PETROLEUM & MINERALS

DHAHRAN, SAUDI ARABIA

In Partial Fulfillment of the
Requirements for the Degree of

MASTER OF SCIENCE

In

MECHANICAL ENGINEERING

April, 2008

KING FAHD UNIVERSITY OF PETROLEUM & MINERALS
DHAHRAN 31261, SAUDI ARABIA

DEANSHIP OF GRADUATE STUDIES

This thesis, written by Abdullah Ali Al-Mesfer under the direction of his thesis advisor, and approved by his thesis committee, has been presented to and accepted by the Dean of Graduate Studies, in partial fulfillment of the requirements for the degree of **MASTER OF SCIENCE IN MECHANICAL ENGINEERING**

Thesis Committee

Dr. Laui Al-Hadrami (Thesis Advisor)

Dr. Mohammed Antar (Member)

Mr. Abdul Quddus Mehruddin (Member)

Dr. Amro Al-Qutub
Department Chairman

Dr. Mohammed Al-homoud
Dean of Graduate Studies

28/1/09
Date

Dedicated to

My beloved parents, whose sacrifices enabled me to reach this stage

Acknowledgments

In the name of ALLAH, the most beneficent and most merciful.

"Verily, my prayer, my sacrifices, my living, and my dying are for ALLAH, the Lord of Alamin (mankind, jinn and all that exists)".

"He has no partner, and of this I have been commanded, and I am the first of Muslims."

All praise to almighty ALLAH Who gave me the patience and perseverance to carry out this research work successfully.

Acknowledgment is due to King Fahd University of Petroleum and Minerals (KFUPM) and its Research Institute (RI) for providing full support to this work.

I deeply appreciate my thesis committee Chairman Dr. L. M. Al-Hadhrami and Dr. M. Antar for their constant help, guidance and the countless hours of attention they devoted throughout this work. My innumerable interruptions into their offices always generated a cheerful response. Thanks to Dr. Al-Hadhrami and Dr. Antar for introducing me to a new dimension in the world of heat transfer.

Thanks are due to my thesis committee members Mr. Abdul Quddus from RI, whose continued help, assistance and guidance made the experimental task manageable. I greatly appreciate his role in achieving my objectives related to the experimental

work. Thanks are due to my friends, especially Mr. Abdurrahman M. Al-Mansour for his unlimited support and understanding, throughout my academic career.

Lastly but not the least, thanks to my parents and wife for their patience and encouragement throughout this work.

Table of Contents

List of Figures

List of Tables

ملخص الرسالة

إسم الباحث : عبدالله علي المسفر

عنوان الرسالة : تاثير حركة الموائع في ترسيب كبريتات الكالسيوم على سطح معدن الألمونيوم

التخصص الرئيسي : الهندسة الميكانيكية

تاريخ الدرجة : مارس 2008 م

إن البحث الحالي يحتوي على تجارب عملية وتحليل بياني لنتائج متعلقه بترسب كبريتات الكالسيوم على سطح معدن الألمونيوم بإستخدام جهاز الألكترود الإسطواني الدوار . وقد لوحظ انه كلما زادت سرعة الدوران، كلما زاد معدل الترسيب على سطح المعدن . بالإضافة الى ذلك تم تصويروفحص تشكّل و توزيع ترسبات كبريتات الكالسيوم على سطح معدن الألمونيوم بإستخدام الفاحص المجهري الإلكتروني، وقد تم إستنتاج انه كلما زادت السرعة كلما زادت قوة إلتصاق كبريتات الكالسيوم بسطح المعدن. كذلك تم دراسة مجموعة من الأبحاث مما تم نشره ا في السابق بخصوص هذا الموضوع و تم عمل مقارنة بين نتائج هذه الدراسة و دراسة سابقة عن ترسيب قشور كبريتات ا لكالسيوم على سطح معدن الفولاذ الصامد (Stainless Steel) في ظروف تشغيل متطابقة.

Abstract

Name: Abdullah Ali Al-Mesfer

Title: Effect of Fluid Hydrodynamics on Calcium Sulfate ($CaSO_4$) Deposition on Aluminum Metal Surface

Major Field: Mechanical Engineering

Date of Degree: March, 2008

This experimental study was conducted using Rotating Cylinder Electrode (RCE) equipment available in the Engineering Research Center of the Research Institute (RI), to investigate the effect of fluid hydrodynamics on Calcium Sulfate ($CaSO_4$) scale deposition on Aluminum metal surfaces. It has been found that the deposition rate increased as the speed of rotation increased. In addition, Scanning Electron Microscopic examinations were carried out to study the morphology and distribution of the $CaSO_4$ crystals deposited on the metal surface. At low speeds, the deposited scale was soft and loose while at higher speed it was compact and hard. Finally, based on the literature review, a comparison is presented of the $CaSO_4$ scale deposition on Aluminum against Stainless Steel (SS-316) at similar experimental parameters, such as solution concentration, speed of rotation and temperature.

CHAPTER 1

INTRODUCTION

Scale formation is a serious and challenging problem encountered in many industries, including oil and gas production. Heat transfer equipment, such as heat exchangers and boilers, is used extensively in several industrial applications, e.g. power generation, refineries, petrochemicals and desalination plants, to exchange heat between two fluid streams. Deposits of scales on tubes reduce their capability to exchange heat, and degrade their efficiency and increase operating cost, and sometime cause catastrophic failure and plant shutdown.

The major factor behind the decreased efficiency of heat transfer equipment is the scale deposition, i.e., buildup of unwanted material on the heat transfer surface that is well known as "Fouling". The scale deposition has very low thermal conductivity which will impose further resistance to heat transfer in addition to those present in any typical design of exchanger. Moreover, pressure buildup will take place due to the flow restriction in the passage of flow because of scale accumulation on the wall surface. Both of these consequences will result in additional energy requirement.

In a laboratory, a methodology was developed earlier to study scale buildup on metal surfaces by using the Rotating Cylinder Electrode (RCE) which simulates the conventional pipe flow [1]. This technique has some advantages over conventional flow loop test methods due to the ease of creating turbulent flow conditions and the simplicity in handling and operating the whole test equipment. In the present research

work, Aluminum test samples were selected since to the author's knowledge no one has investigated such material with the RCE apparatus at different rotational speed (RPM) and surface roughness, to study the effect of fluid hydrodynamics on the $CaSO_4$ scale deposition on Aluminum sample surface. From the mathematical equation introduced by Gabe [2] it is clear that Reynolds number (Re) and the rotational speed are directly proportional. As rotational speed increases, the Reynolds number increases too.

The boundary conditions in conventional flow loop are V = 0 at pipe wall, V= maximum at the middle. However, for RCE $\omega = 0$ at cylinder stationary wall, ω = maximum at rotating cylinder wall, the inner cylinder is rotating and the outer is stationary. Scientists have concluded that, for mass transfer equation of both geometries, the dependence of wall shear stress on Reynolds number is the same and the hydrodynamics boundary layer is much bigger than mass transfer boundary layer. Because of the high Schmidt (Sc) number which is normally encountered in liquid, the conditions of equality of mass transfer coefficients can be established and solved for RCE velocity which duplicates the mass transfer coefficients in pipe flow geometry. Also, temperature and hydrodynamics conditions must be the same, i.e. turbulence.

1.1 Literature Review

Fouling results from the accumulation of particles suspended in liquid or gaseous streams onto heat transfer surfaces [3]. Sometimes, the particles accumulate due to gravity, which is referred to as sedimentation. The suspended particles may

include ambient pollutants, like sand, iron material, microbial organisms in cooling water, and airborne particles in an air-cooled heat exchanger. For example, when river water is used as a cooling medium, particles of clay and mineral matter are carried into the river by run-off, and the subsequent concentration can be high or low depending on local rainfall conditions. When a metallic heat transfer surface is exposed to a corrosive liquid medium, the products of corrosion can foul the surface, provided the pH of the medium is not so strong as to dissolve the corrosion products as they are formed. Corrosion will take place once the surface is brought into contact with the corrosive medium. Corrosion is so powerful that its effect is observed immediately and appears faster than the other fouling types. This type of corrosion may degrade the heat transfer surface, thus leading to a leak that could cause fire or interrupt the operation. As a result of corrosion, in a heat transfer system, the corrosion products may be released into the flowing stream either in particulate form or as dissolved species. The material may then be deposited on heat transfer surfaces, and the resultant fouling is ex-situ. Conversely, corrosion fouling on the heat transfer surface is known as in-situ corrosion. The biological type of fouling is due to the development and deposition of organic films consisting of micro-organisms, such as barnacles and mussels. Because such fouling involves living matter, the temperature range over which it can exist is limited to 0-90 ^{o}C. The highest concentration occurs roughly in the range from 20 ^{o}C to 50 ^{o}C. Excessively thick layering of biological material is possible under certain conditions. In cooling water systems particularly, the presence of biofilm may promote other fouling processes such as corrosion. For instance, pitting corrosion is quite commonly formed under a slime layer.

Precipitation fouling is the deposition of a solid layer on a heat transfer surface. It occurs when the process conditions lead to supersaturation of the dissolved

inorganic salts at the heat transfer surfaces. These process conditions involve evaporation beyond solubility limits, or cooling/heating beyond solubility limits, or mixing of the process stream. The industrial systems and operations where precipitation fouling is of major significance are Saline Desalination Plants, Geothermal Brine Systems, Cooling Water Systems, Steam Generation Systems and Potable Water Supply Systems. Some dissolved species show inverse solubility versus temperature behavior. In this case, the substance tends to precipitate on a heated rather than a cooling surface as seen in cooling water application. As explained in this study, $CaSO_4$ is one of the salts that exhibit this behavior. The driving force for crystallization is the chemical potential difference between the substances in the solution and the deposit formed on the metal surface [3].

Neusen et al. [4] discussed the effect of supersaturation, pH, Reynold number and concentration of ions in the brine solution on the formation of silica scale in heat-exchanger tubes, and they proposed a silica deposition model. Chemical reaction fouling includes deposits that are formed as a result of chemical reactions within the process fluid. Although the heat exchanger surface does not act as a reactant, it sometimes behaves as a catalyst [5]. This type of fouling commonly occurres in chemical process industries, refineries, and dairy processes.

Neville et. al. [6] studied the nucleation and growth of $CaCO_3$ scale on SS-316L metal surface in supersaturated solution using a rotating disc electrode (RDE). Their method was based on the correlation between the diffusional characteristic of oxygen at a metal surface and the change in the rate of oxygen reduction once nucleation and growth of the $CaCO_3$ starts. They found that the technique successfully helped in the assessment of the scale buildup on metal surface, and when compared

with the result from image analysis they showed similarity especially at high surface coverage.

Chen et. al. [7] studied scale formation and adhesion on stainless steel-316 metal surfaces through an electrochemical technique, which monitored the scale coverage by measuring the oxygen reduction on the sample under potentiostatic control. They found that the precipitation in the bulk solution is affected by concentration of ions in solution. For bulk precipitation, higher concentration takes a shorter induction period (the time between supersaturation creation and the first observable change in the solution's physical properties). The scale morphology examinations of the bulk solution and the metal surfaces showed that of the crystals formed in the bulk solution are smaller by almost half or even less than those formed on the metal surface. Also, they noticed that the surface coverage was ranged from 70-80 % after some hours.

Quddus and Allam [8] studied the deposition of $BaSO_4$ scale on a stainless steel sample (SS 316) using the RCE apparatus. They noticed that as the Reynolds number increases, so too does the rate of scale deposition on the electrode surface, which proves that the process is diffusion controlled. The morphology examination of the scale using Scanning Electron Microscopy (SEM) reveals that the $BaSO_4$ crystals were dense and uniformly distributed over the metal surface. This was in agreement with a previous study for the $SrSO_4$ scale formation [9].

Quddus [10] investigated the $CaSO_4$ deposition on 316-stainless steel sample using the RCE, and found that $CaSO_4$ scale deposition on a metal surface is proportionally influenced by the Reynolds number, which means that the higher the

speed of rotation the more scale deposition on the metal surface. This is in agreement with the above cases of $BaSO_4$ and $SrSO_4$. However, examining the scale crystals using the SEM revealed that the $CaSO_4$ crystals initially grow perpendicular to the substrate and then branch out randomly in all directions. This was considered a typical characteristic of $CaSO_4$, but the crystal structures of $BaSO_4$ and $SrSO_4$ scales did not experience this pattern.

Neville and Morizot [11,12] studied scale build-up on steel using RDE apparatus under application of cathodic protection in three different solutions. They noticed that, for a solution containing Magnesium (Mg) and Calcium (Ca) ions, a densely packed fine crystal basal layer (thin layer) rich in Mg was formed which contained needles identified as Aragonite (a form of $CaCO_3$). For the solution that did not contain Ca, a similar deposition occurred, except that the needles crystals were absent. In the solution without Mg ions, the growth of $CaCO_3$ is promoted and the scaling crystal characteristic is of Calcite (another form of $CaCO_3$ scale). From the above, it was noticed that the existence of Mg ions in the solution encouraged the formation of Aragonite and prevented the Calcite structure.

Gabe et al. [13] reviewed the use of the RCE in electrochemistry from 1982 to 1995. Different geometries (namely rotating cylinder electrode, rotating cone electrode, rotating hemispherical electrode, rotating wire electrode and rotating disk electrode) were covered in their review, and they found that the RCE was generally accepted and increasingly widely used. Also, the mass transported to the electrode can be altered and controlled by diverse factors including surface roughness, and the higher roughened surfaces attract more scales than the smooth surfaces. In addition, the log-log plot of the Sherwood number (Sh) versus the Reynolds number, which is

used to show the mass transport to the metal surface, has a continuous linear relationship where the electrode surface is smooth. However, for a rough electrode surface, the relation between Sherwood and Reynolds numbers is nonlinear and has a discontinuity after a particular Reynolds number.

Branch and Muller [14] studied the influence of scaling on the performance of shell and tube heat exchangers. They modeled the fouling mechanism by combining Hassons's ionic diffusion model for scaling with the Gaddis and Schlunden model for predicting the temperature distribution. They found that scaling can be predicted even with a negative temperature difference between the heat transfer surface and the working fluid. This is due to the high supersaturation of the fluid, which induces the mass transfer regardless of the opposite driving force resulting from the negative temperature difference. In addition, they noticed that when scaling took place in all four configurations of the heat exchanger, there were no major differences in the temperature distribution among the different patterns. This is opposite to the case of clean exchangers, where each configuration has its own temperature distribution.

Fahiminia et al. [15] studied experimentally the effect of temperature and velocity on the inverse solubility rate of $CaCO_3$ at the initial scaling under sensible heating condition (no vaporization). The bulk inlet temperature was 55 ^{o}C while the clean surface temperatures were varied from 80 to 101 ^{o}C, and the Reynolds number varied from 7000 to 21000. Under all these conditions, they found that the delay time (the period between the occurrence of supersaturation and the first detection of fouling deposition on the metal surface) is influenced by surface temperature and velocity. As the bulk temperature and velocity increases, the delay time decreases for

velocities below about 0.5 m/s but it remains approximately constant at higher velocities.

Sheikhholeslami and Ng [16] studied the fouling of heat exchangers under co-precipitation (solution containing both salts) of inorganic salts. They investigated and quantified the co-precipitation process of $CaCO_3$ and $CaSO_4$ when sulfate SO^-_4 is the dominant anion. They observed no induction period associated with coprecipitation, and scaling began almost immediately. Also, they noticed that the precipitation was fine, with a loosely adhering layer for pure $CaSO_4$. Moreover, as the concentration of $CaCO_3$ increased, it tended to be and more strongly adherent. For the solution containing only pure $CaSO_4$, the precipitate had long needle-shaped crystals floating in the solution. When $CaCO_3$ was added with a concentration of 0.002 moles, the needle-shaped crystals got shorter and adhered more strongly to the tube surface. As it increased above 0.008 moles, the precipitation became fine powder white crystals with small needle-shaped crystals. The temperature increase raised the precipitation rate of both $CaCO_3$ and $CaSO_4$.

Behbahani et al. [17] investigated the tube side fouling of heat exchangers exposed to a solution of calcium sulfate ($CaSO_4$) dissolved in a high concentration of phosphoric acid (H_3PO_4). The results showed that for the range of solution velocity (1.3-1.8 m/s) there was an inverse linear relationship with fouling resistance. This linearity was generally an indication of hard and adherent deposits, and it implied that the deposition rate was constant or no removal occurred, or the difference between deposition rate and removal rate was constant. The second factor that was investigated is the surface temperature of the tube. As the surface temperature increased, the fouling resistance rose. In addition, the change in fouling resistance was sensitive to

even a small change in surface temperature. Fouling resistance increased as the degree of solution supersaturation increased. Finally, it was concluded that the fouling process was a chemically controlled reaction.

Helalizadeh et al. [18] have studied experimentally the effects of various operating parameters, such as solution composition and hydrodynamics of the system, on the crystallization fouling of the mixtures of calcium sulphate and calcium carbonate under convective heat transfer and sub-cooled flow boiling condition. This was achieved by conducting experiments under controlled conditions where certain parameters were constant or where their effects were minimized. Those authors found that the resulting scale depends on both salts in terms of ions concentration. The fouling crystallization during the formation of bubbles on the heat transfer surface was high, and salts concentration below the bubbles increased significantly, which resulted in the formation of the deposit on the heat transfer surfaces. The bubbles formation disturbed the boundary layer, which increased the mass transfer coefficient and led to more deposition or formation.

Yang et al. [19] investigated the induction period (the time between supersaturation creation and first observable change in solution physical properties) of the $CaCO_3$ fouling on a copper surface compared with a heated Self-Assembled Monolayer (SAM) which is ultra thin, low energy, well defined, ordered organic film formed on solid surfaces by adsorption of amphiphilic organic molecules from solution). They also studied the morphologies of $CaCO_3$ in the presence and absence of the antifouling polyacrylic acid (PAA). At a constant initial surface temperature and similar experimental conditions, the SAM material experienced an induction period of one hour, while there was no induction period for copper. As the velocity

increased, more foulant ions diffused to the surface, which minimized the induction period. When both fluid velocity and initial surface temperature were considered at the same time, the initial surface temperature influenced the induction period more than fluid velocity did. The scale morphology of the $CaCO_3$ on the SAM surface was in the forms of Calcite or Aragonite (forms of $CaCO_3$ scale). For the copper material, the $CaCO_3$ scale formed in the presence of the antifoulant PAA lost its sharp edges.

Klaren et al. [20] proposed a novel design of shell and tube heat exchanger which employs a self-cleaning principle. This new design consists of two parallel tube bundles inside one shell with the foulant process streams passing through these tubes. A clean intermediate fluid operating in the shell-side which comprises both bundles transfers the heat between both bundles. As a result, the zero fouling self-cleaning heat exchanger required only one-third of the heat transfer surface area needed by the conventional type. A much longer period of operation can thus be achieved between inspections or cleanings. Also, the pumping power required for the zero fouling self-cleaning heat exchanger is less than that for the conventional heat exchanger.

Liu et al. [21] examined the relationship of corrosion in a rotating disk system and in a turbulent pipe flow system. A closed-form mathematical model was developed in order to predict the turbulent pipe flow based on the rotating disk experiments. The resultant model was in good agreement with experimental results of other researchers. Eventually, the pipe corrosion can be predicted using easily obtained experimental data via the rotating disk electrode.

Efrid et al. [22] quantified the relationship between laboratory fluid flow data corrosion test techniques and field application to define the parameters required to

apply laboratory data effectively to field operations based on carefully generated corrosion data. They used jet impingement and RCE techniques, which were compared directly to simultaneous pipe flow experiments. They found that the RCE technique provided stable and reproducible turbulent flow with relatively small volumes of test fluid, and could not be used for high pressure or high temperature applications or even for gas and gas/liquid systems. They found that the basic equation for the effect of wall shear stress on carbon steel, which relates the rate of corrosion to wall shear stress, is suitable for corrosion prediction.

Silverman [23] presented the investigation that he made by using different geometries of rotating electrodes, Rotating Cylinder Electrode (RCE), Rotating Disk Electrode (RDE) and Rotating Hemisphere Electrode (RHE). He found that RCE is the best geometry to predict scaling in pipe flow by equating the mass transfer rate, since both geometries operate under a turbulent flow regime, where a direct quantitative relation always exists between the mass transfer rates and Sherwood number or with the product of Reynolds and Schmidt numbers.

Ashiru and Farr [24] used the electrode hydrodynamics technique to provide kinetic information concerning electrodeposition of silver from iodide and cyanide electrolytes which were prepared at the laboratory. They found that the electrode hydrodynamics technique shed some light on the cathodic discharge current and the associated reaction path during silver deposition. They concluded that the silver electrodeposition using the electrode hydrodynamics RCE or RDE techniques is more practical than the ordinary method for silver deposition.

Khokhar et al. [25] performed a series of experiments to study the effect of rotation speed on the deposition of strontium sulfate, which is one of the common scales found in the oilfield deposits. They observed that the scale deposition rate increased with the increasing Re for both laminar and turbulent regimes, and they found it to be three times higher for turbulent than laminar flow. They also noticed that the deposition rates on the pre-scaled samples are higher than those on the bare ones and increased with higher surface roughness.

Neville et al. [26] conducted an experimental study based on an electrochemical technique that uses the assessment of the oxygen reduction reaction at a rotating disk electrode, to examine its suitability for scale deposition studies. They found it a promising method for studying the nucleation and growth of the scale at a solid surface, and they found it to be effective in predicting the scale coverage on the metal surface. They confirmed their results by comparing the predicted coverage with direct calculations of scale morphology by SEM integrated with image analysis to verify actual percentage surface coverage.

1.2 Objectives

The objective of this study is to investigate the deposition rate and morphology of Calcium Sulfate ($CaSO_4$) on Aluminum metal surfaces. $CaSO_4$ is considered as one of the most commonly found scales in Arabian Gulf water used in the cooling of the industrial plants and facilities. From the literature review, the author infers that no previous research has reported the $CaSO_4$ deposition on Aluminum metal surface in the petroleum industry.

The apparatus for the present research is known as RCE, which is available in the Corrosion laboratory of the Research Institute at KFUPM. This device simulates the flow in tube geometry. The experimental work was done by using two sets of Aluminum test samples. Each set was polished to a determined surface roughness. The samples were immersed in a supersaturated solution, and the speed of rotations was varied, to investigate the different Reynolds numbers resulting from varying the speed of rotation on the scale deposition on that metal surface.

Almost all the Reynolds numbers resulting from the selected speed of rotations were considered turbulent (turbulent $\geq$ 200 RPM). The two surface roughness sizes that were used to polish the test samples were 120 and 600 grit size. Throughout this report, the two grades of polished samples are called respectively 600-G and 120-G. The 600-G size is considered as soft compared to the 120-G size. The morphology examinations using the SEM were conducted to study the scaling structure shape after deposition. The final results were compared against the earlier outcomes by Quddus [10], who investigated the deposition of $CaSO_4$ scale on Stainless Steel 316 metal samples under the same experimental conditions. The objective of this comparison between these two metals is to see which one would perform better in terms of scale build-up resistance.

The results of this study are intended to help the engineers who work in the design and manufacturing of process equipment. It is hoped that the present study will help them select the proper material under same range of hydrodynamic conditions investigated in this work.

CHAPTER 2

EXPERIMENTAL WORK

2.1 Experimental Setup

The RCE is a well established device for studying kinetics of corrosion [21-23] and electrodeposition [24]. It has been used for investigating the scale deposition on metal surfaces [25, 26] in laboratories. The RCE has some advantages over the conventional flow loop for studying the scale buildup, due to its simplicity for establishing turbulent flow condition at lower agitation rates [24, 25], and controlled hydrodynamic conditions.

The RCE components used in the experiments are shown in Figure 2.1. The Aluminum samples (5) were fitted on the Teflon coated shaft (3) and secured with the Teflon cap (6). The Teflon ring (4) was used for ease of removal of the sample after each run. The shaft was attached to the rotating motor (2) to provide the required rotational speed. Then The shaft with the samples together were immersed in the glass cell (7) that contained the supersaturation solution. The solution was supplied to the cell from the plastic translucent reservoir (1). All the experiments were conducted at the 60 ºC temperature and atmospheric pressure.

The plastic translucent reservoir which contained the $CaCl_2$ and Na_2SO_4 supersaturation solutions had a volume of 4 liters. It is connected to the cylindrical

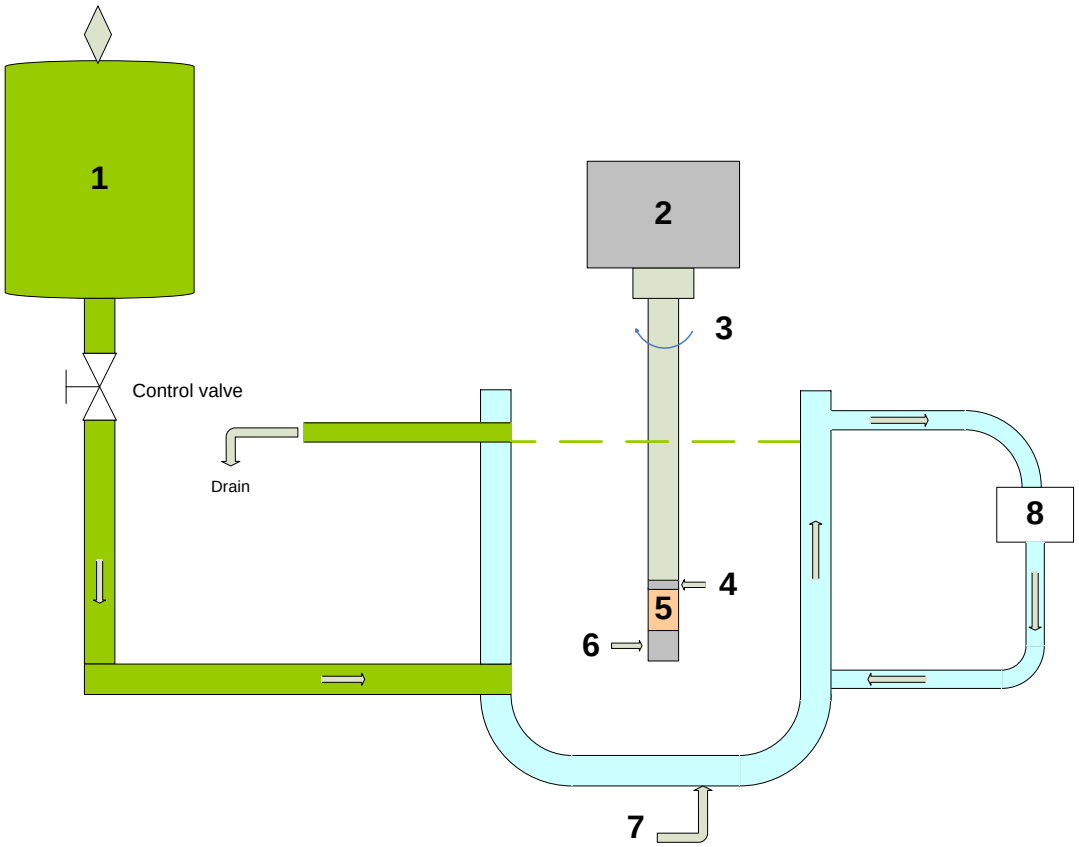

1	Supersaturation reservoir	5	Sample
2	Motor to rotate sample at preset rpm	6	Teflon cap
3	Teflon-coated shaft	7	Glass test cell (double wall)
4	Teflon ring	8	Hot water circulation bath

Figure 2.1: Schematic of Experimental RCE Apparatus

double wall heat exchanger cell via 1/4 translucent tubing. The cell is 13.0 cm long with inner diameter of 3.4 cm.

The samples were rotated inside the glass cell by EG&G (Princeton Applied Research) Rotating Disk Equipment Model 616, which enabled the rotation speed to be varied from 1 to 9999 RPM. The rotation speeds in our experiments were in the range of 50 to 2000 RPM.

2.2 Aluminum Samples Preparation

The cylindrical test samples, 0.5 inch (1.27 cm) long and 0.5 inch (1.27 cm) in diameter, were machined from commercial grade Aluminum. A central hole was drilled in the samples as shown in Figure 2.2 to fit them onto the Teflon coated shaft of the RCE apparatus. The samples were fitted on the lathe machine using a special adapter fabricated for this purpose as shown in Figure 2.3 and Figure 2.4. Then they were polished to the desired roughness with the 120-G and 600-G carbide (SiC) paper. After polishing, they were thoroughly degreased with acetone and rinsed with distilled water. They were secured tight on the shaft with the help of a Teflon end-cap. Thus the sample became a part of the long cylinder shaft, exposing only the peripheral surface of the sample to the supersaturated solution. For each experiment, a fresh polished sample was used.

2.3 Solution Preparation

The supersaturation solutions were prepared by adding respectively 176.424 g of $CaCl_2.2H_2O$ and 170.448 g of Na_2SO_4 salts into 20 liters of distilled water. The salts were added gradually to the water in a beaker which was placed on a stirrer device.

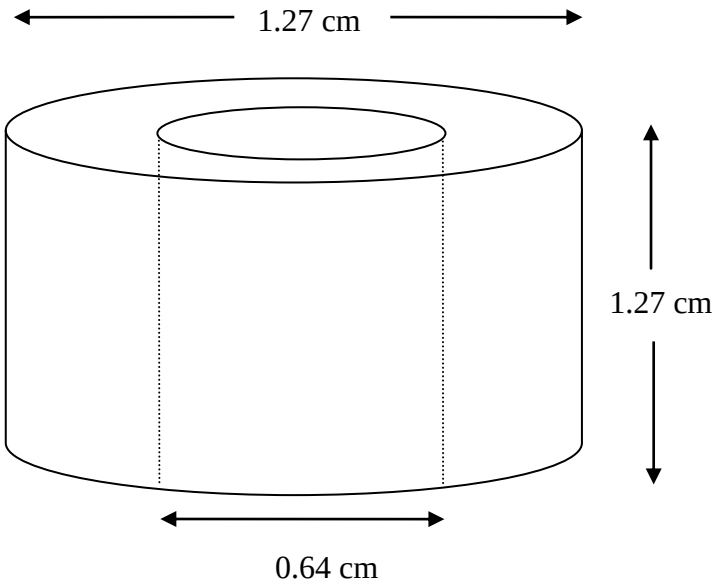

Figure 2.2: Dimensions of Aluminum Sample

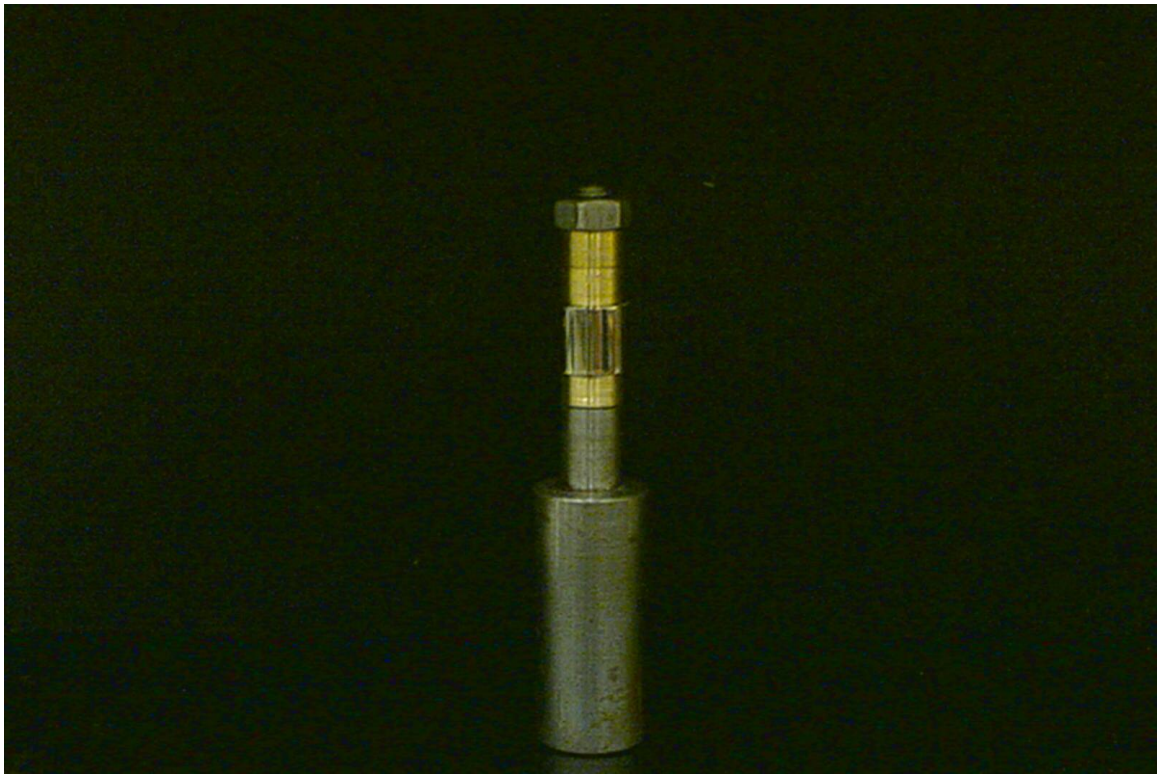

Figure 2.3: Picture of Sample Adaptor

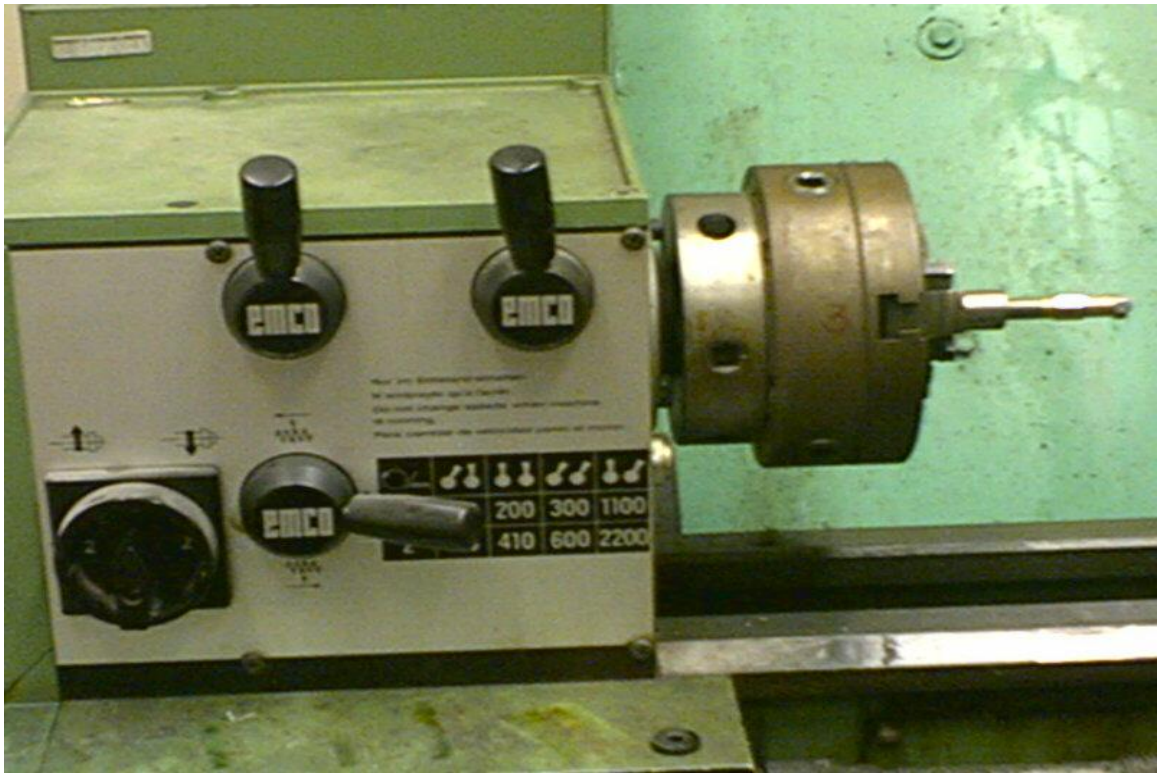

Figure 2.4: Picture of Adaptor with Sample Fitted on Lathe Machine for Polishing

to dissolve the salts and achieve proper mixing. The process was continued until the desired amount of the two volumes of $CaCl_2$ and $NaSO_4$ solutions were prepared. Whenever additional solution was needed, the above procedure was repeated to produce the required quantity.

The two equal volumes of reactant solution were mixed in a translucent reservoir bottle and shaken very well. The mixed supersaturation solutions provided a certain predetermined molarity of 0.03 mole/liter of $CaSO_4$. The mixed solution was transferred to the heat exchanger glass cell, where it was heated to 60 ºC by a hot water circulation bath to produce scale precipitation according to the following chemical reaction:

$$CaCl_2.2H_2O + Na_2SO_4 \rightarrow CaSO_4 + 2NaCl + 2H_2O \qquad \textbf{(2.1)}$$

2.4 Experimental Procedure

All the experiments were conducted using the following procedure. First, to heat the solution, the water bath heater (a machine with pre-setting temperature control, which is filled with water and has an internal coil to heat the water) was switched on with a preset temperature of 60 °C as in the previous study [8,10] so that the results can be compared. The solution was heated by the constant temperature water, circulating through the jacket surrounding the double-wall glass cylindrical cell. The water in the jacket was circulated by a constant temperature water-circulating arrangement as shown in Figure 2.1. All test experiments were performed at 60° C temperature under atmospheric pressure. The duration of each experiment was set at six hours, as in previous research [8,10] and found adequate for scale

deposition on the surface of the sample. At the start of each experiment, the sample was thoroughly cleaned with distilled water and acetone, and then weighed and mounted on the shaft of the rotating equipment. At the end of each experiment the sample was gently rinsed with water and acetone, carefully removed from the shaft, dried in the oven for two hours, and re-weighed to determine the scale gained by the sample. An analytical balance with an accuracy of ± 0.1 mg was used to check the weight gain of the scale on the sample.

The supersaturated solution contained in the reservoir was allowed to flow slightly drop by drop at a rate of about 1.5 liter/hour to the double wall glass cell which acted as a heat exchanger (Figure 2.5). It was kept for almost 10 minutes in the cell before immersing the sample so that the temperature of the solution reached a steady 60°C. After that, the sample attached to the rotating equipment was immersed in the solution inside the cell, and the test was started by operating the rotating equipment with a predetermined selected speed. The outlet tubing was opened to drain off the overflow. The supersaturated solution in the reservoir bottle was replenished when necessary by adding an equal volume of $CaCl_2$ and Na_2SO_4 solutions. The continuous flow of the fresh solution to the cell ensurred that the sample was exposed to a solution of constant composition during the experiment run. All the experiments were monitored during the test to take care of anything unexpected e.g. solution running out, inner tube scale buildup or drain blockage. The reservoir and glass cell were cleaned with diluted HCl and distilled water after each run to get rid of any contaminants.

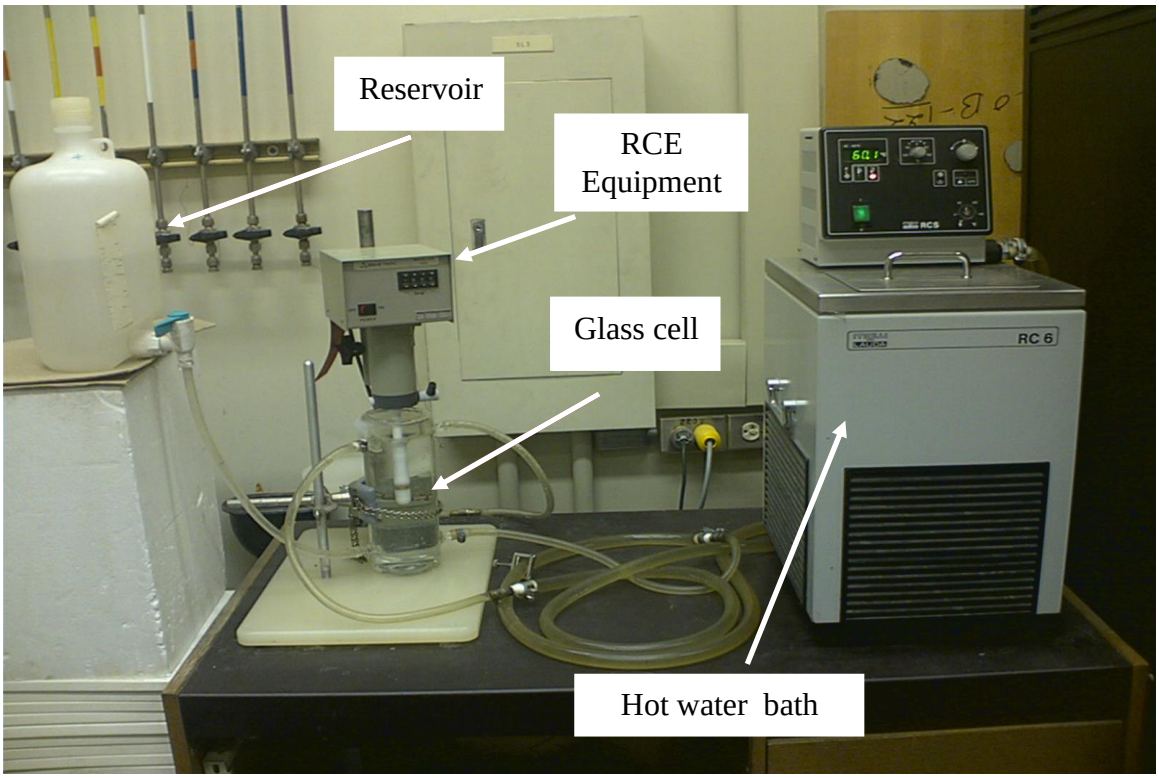

Figure 2.5: Rotating Cylinder Electrode (RCE) Apparatus Components

2.4.1 Measurement of Surface Roughness

The surface texture of the 120 and 600 grit polished Aluminum samples was determined by using the Bendix Linear Profile system, Model 5054. The measurements were performed at 20 ºC ± 0.5 ºC and relative humidity (RH) of 40% ± 5 %. The average roughness of the test samples was measured using the linear profiling system which consisted of a console-mounted pilotor, a tracer diamond stylus, a profiling amplifier and a strip chart recorder. The pilotor provided a straight line datum axis, and it moved the tracer along the surface of the workpiece placed on the surface of the console. As the tracer stylus was displaced by the irregularities in the past surface, electrical signals from the tracer were amplified, filtered and recorded on a strip chart. The surface roughness of the piece was measured both in forward and reverse direction of the tracer.

2.4.2 Procedure for Studying Morphology of $CaSO_4$ Scale

The morphology of calcium sulfate crystals was studied by using flat aluminum coupons having dimensions of 20 mm by 8 mm by 1.5 mm. The coupons were polished to 120-G and 600-G with SiC paper. After polishing, they were thoroughly degreased with acetone and rinsed with distilled water. Duplicate samples were assembled in a Teflon holder that was placed in the test cell where they were exposed to the calcium sulfate scale-forming solution for 1 to 6 hours under the same test conditions mentioned above. After the tests, the coupons were retrieved, rinsed with distilled water, dried in an oven, and preserved for the SEM examination to reveal the morphology of the hydrodynamically deposited crystals of $CaSO_4$ on the Aluminum substrate surface. The JEOL model JSM 5800 LV SEM fitted with EDS was used for the $CaSO_4$ crystals morphological study.

2.4.3 Procedure for Solution Comparison Determination

Before entering and after exiting the heated cell, the solution was analysed to compare the scale forming solution. Ion chromatography was used to determine chlorides and sulfates. Total dissolved solids (TDS) were determined gravimetrically, while the metals were determined by Inductively Coupled Plasma – Atomic Emission Spectroscopy (ICP – AES) techniques.

2.4.4 Procedure for Determination of Induction Time

The induction time is defined as the time between the creation of the supersaturation solution and the first observable scale on the metal surface. The induction period was determined by conducting deposition experiments as a function of time at certain selected RPM, with identical other experimental conditions adapted for current work. The result was plotted as deposition verses time, and the required induction time was calculated using linear extrapolation towards time axis (x-axis) and its intercept with the time axis was taken as the onset of scale deposition on the sample.

CHAPTER 3

UNCERTAINTY ANALYSIS

3.1 Data Reduction Equation

The weight gain (W_g) of the sample was calculated as its weight in grams after the test minus its initial bare polished weight measured up to four decimal places. This difference was divided by the product of the sample surface area measured in square meters and the test duration measured in hours. The final result is therefore expressed as g. m^{-2}. h^{-1}.

The reduction equation used to calculate the deposition rate is shown below:

$$D_r = W_g * A_s^{-1} * t^{-1} \qquad \textbf{(3.1)}$$

D_r Deposition rate ($g.m^{-2}.h^{-1}$)

W_g ($W_{after} - W_{before}$) Weight gained by sample measured in gram (g)

As Cylindrical surface area of the sample, [π.D.L] (m^2)

t The duration of the experiment measured in hour (h)

L Length of the sample (m)

The W_g is the weight gain by the sample after deposition of $CaSO_4$ scale measured in grams. The As is the surface area exposed to the solution measured in square meters and t is the duration of each test measured in hours. The equation used for calculating the Reynolds number was developed earlier by Gabe [2] :

$$Re = R_1 \omega [(R_2-R_1)/\nu] \qquad \textbf{(3.2)}$$

Re Reynolds number

R_1 Sample outer radius (cm)

R_2 Cell inner radius (cm)

ν Kinematics viscosity of solution (cm^2/s)

ω Rotational speed (rad/s)

In this equation, R_1 is the sample outer radius from the center of the Teflon shaft measured in centimeters. R_2 is the inner radius of the glass test cell measured in centimeters. The kinematics viscosity ν was measured in square centimeters per second, and the rotational speed (ω) in radians per second.

3.2 Uncertainty Analysis

The uncertainty analysis equations used in the present work were developed by Coleman and Steele [28], which include the precision, bias, and the resultant uncertainty. The bias errors are often neglected in books and articles in error analysis or uncertainty analysis by a simple assumption that "*all bias errors have been eliminated by calibration*". Therefore we consider the precision uncertainty only to calculate the amount of uncertainty in the current experimental investigation. The method for performing the uncertainty analysis in the present experimental investigation was proposed by Taylor [29]. The theory for the current uncertainty analysis is summarized below.

The uncertainty analysis is associated with experimental results determined by using a data reduction equation. The measurements of the variables (W_g, L, D, and t) in our case have uncertainties associated with them. The uncertainties of each individual variable propagate through the data reduction equation into the result, and

are calculated using uncertainty analysis. In general, an experimental result, *r*, is a function of j variables X_i

$$r = r\,(X_1, X_2, \ldots\ldots, X_J) \qquad \textbf{(3.3)}$$

Equation (3.3) is the data reduction equation used for determining r from the measured values of the variables X_j. Then the uncertainty in the result is given by

$$U_r^2 = \left[\left(\frac{\partial r}{\partial X_1}U_{x1}\right)^2 + \left(\frac{\partial r}{\partial X_2}U_{x2}\right)^2 + \ldots\ldots\ldots\ldots + \left(\frac{\partial r}{\partial X_J}U_{xj}\right)^2\right] \qquad \textbf{(3.4)}$$

Where

U_{x_j} = The uncertainties in the measured variables X_j.

No general discussion of errors can be complete in listing the elements contributing to error in a particular measurement. In the discussion below, errors are grouped into two very general categories (Figliola [30])

1. Bias error
2. Precision error

The total error in a single measurement is the sum of the bias and the precision errors in that measurement. The total error contained in a set of measurements obtained under seemingly fixed conditions can be described by an average bias error and a statistical estimate of the precision errors in the measurements.

3.2.1 Uncertainty in Deposition Rate

Now we present the uncertainty for the scale deposition rate generated from the current study. The Reynolds number and the deposition rate are functions of many parameters such as:

$$Re = f(R_1, R_2, \omega, \nu) \qquad \textbf{(3.5)}$$

and

$$W_g = f(\Delta T, Re, t) \qquad \textbf{(3.6)}$$

Taking into consideration only the measured values, which have significant uncertainty, the deposition rate is a function of

$$D_r = f(\Delta T, \rho, \omega, D, \mu, t, L) \qquad \textbf{(3.7)}$$

where all variables are measured except the constant pi (π), and the Re number is directly proportional to the weight gain W_g, and its contribution to the error is apparent, since the scaling process is diffusion controlled. Below is a more simplified form of the reduction equation:

$$D_r = \frac{W_g}{(\pi * D * L) * t} \qquad \textbf{(3.8)}$$

Now, the standard uncertainty in the deposition rate as given in equation 3.8 is calculated using the following equation:

$$U_{Dr}^2 = \left(\frac{\partial D_r}{\partial W_g} U_{Wg}\right)^2 + \left(\frac{\partial D_r}{\partial D} U_D\right)^2 + \left(\frac{\partial D_r}{\partial L} U_L\right)^2 + \left(\frac{\partial D_r}{\partial T} U_t\right)^2 \qquad \textbf{(3.9)}$$

The uncertainty propagation for the dependent variable in terms of the measured values is calculated using the Engineering Equation Solver (EES) software. The measured variables x_1, x_2 etc., have a random variability that is referred to as their uncertainty. This uncertainty is displayed as ($a \pm u_x$). The input to EES software for calculating the uncertainty of a dependent variable is the magnitude of the measured variable and the uncertainty in each measured variable. Figures 3.1 and 3.2 below depict a sample for writing and calculating the uncertainty for the D_r using the EES software.

3.3 Sample Calculations of Uncertainty

3.3.1 Summary of Uncertainty for the 120-G Surface

Table 3.1 is a summary table for uncertainty analysis results for all deposition rate measurements of the 120-G samples. The detailed calculation of each reading is presented in Appendix-A. From the table, the percentage uncertainty ranges from a minimum value of 2.12 % to a maximum of 2.99 %.

3.3.2 Summary of Uncertainty for the 600-G Surface

Table 3.2 is a summary table for uncertainty analysis results for all deposition rate measurements of the 600-G samples. The detailed calculation of each reading is presented in Appendix-A. From the table, the percentage uncertainty ranges from a minimum value of 2.54 % to a maximum of 4.25 %.

3.3.3 Summary of Uncertainty for Reynolds Number

Table 3.3 summarizes the uncertainty analysis of all Reynolds numbers. The complete calculation is shown in Appendix A. The range of uncertainty percentage is very small; it ranges from 2.02 % to 2.26 %.

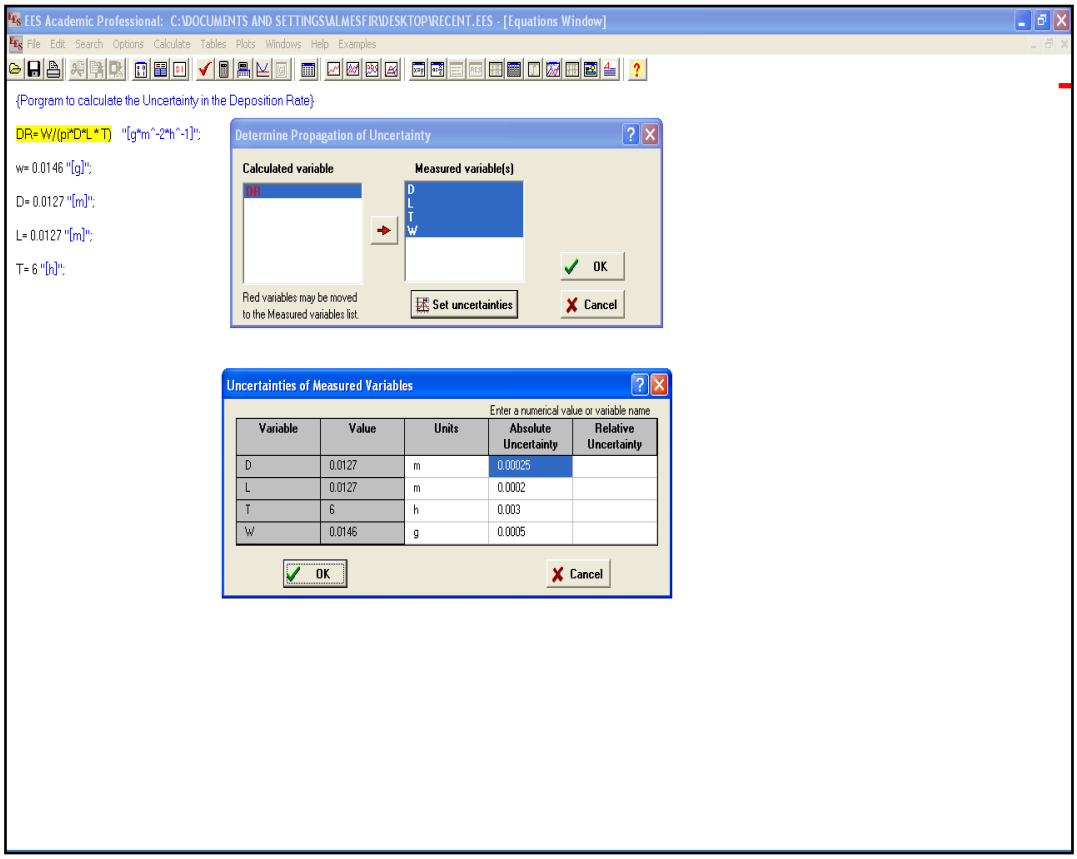

Figure 3.1: Sample for Writing the Uncertainty of Deposition Rate (D_r)

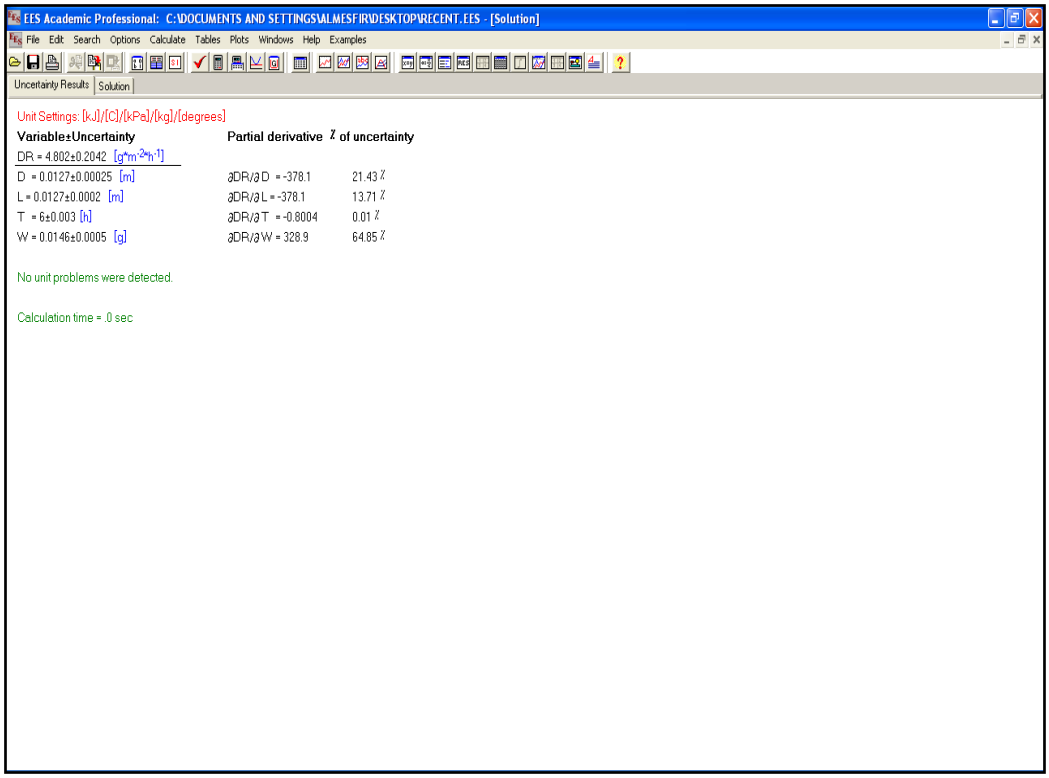

Figure 3.2: Sample Calculation for the Uncertainty of Deposition Rate (D_r)

Table 3.1: Summary of Uncertainty for 120-G Aluminum Samples

Sr. #	Speed (rpm)	Equivalent Re	D_r (g m^{-2} h^{-1})	% Uncertainty
1	50	746	10.291	2.99
2	100	1492	12.248	2.86
3	250	3730	20.91	2.64
4	500	7460	31.168	2.58
5	750	11190	42.51	2.55
6	1000	14921	61.678	2.12
7	1250	18651	76.966	2.53
8	1500	22381	81.996	2.53
9	1750	26111	82.576	2.53
10	2000	29841	84.143	2.53

Table 3.2: Summary of Uncertainty for 600-G Aluminum Samples

Sr. #	Speed (rpm)	Equivalent Re	D_r ($g\ m^{-2}\ h^{-1}$)	% Uncertainty
1	50	746	4.800	4.25
2	100	1492	8.778	3.14
3	250	3730	11.622	2.89
4	500	7460	23.672	2.62
5	750	11190	39.749	2.56
6	1000	14921	56.187	2.54
7	1250	18651	58.259	2.54
8	1500	22381	58.949	2.54
9	1750	26111	59.837	2.54
10	2000	29841	60.527	2.54

Table 3.3: Summary of Uncertainty of Equivalent Reynolds Numbers

Sr. #	Speed (rpm)	Equivalent Re	% Uncertainty
1	50	746	2.26
2	100	1492	2.16
3	250	3730	2.13
4	500	7460	2.12
5	750	11190	2.12
6	1000	14921	2.12
7	1250	18651	2.12
8	1500	22381	2.08
9	1750	26111	2.06
10	2000	29841	2.02

RESULTS AND DISCUSSION

4.1 Measurement of Surface Roughness

Figures 4.1 and 4.2 show the surface roughness of the 600-G and 120-G polished samples, measured by the Bendix Linear Profiling system. The least count (line spacing between two consecutive parallel lines) of the 600-G is 5 μ inches (0.127 μ meters) whereas the 120-G has a least count of 10 μ inches (0.254 μ meters). The average roughness (Ra) values calculated from these charts are summarized in Table 4.1. As seen from Figure 4.1, the average surface roughness of the 600-G is 70 μ inches (1.78 μ meters) in forward travel and 82.5 μ inches (2.09 μ meters) in the reverse travel of the stylus. The surface roughness values for the 120-G is 120 μ inches (3.05 μ meters) and 100 μ inches (2.54 μ meters) for forward and reverse travel, as in Figure 4.2. The line spacing for the surface profile of 120-G is double that of the 600-G. The lower value of Ra indicates relatively smooth surface texture having less waviness compared to higher value of Ra that shows large peaks and valleys, indicative of a coarse or rough surface profile. Based on the surface profile measurements summarized in Table 4.1, the 600-G has a comparatively smooth surface, while the 120-G polished sample has a coarse and rough surface.

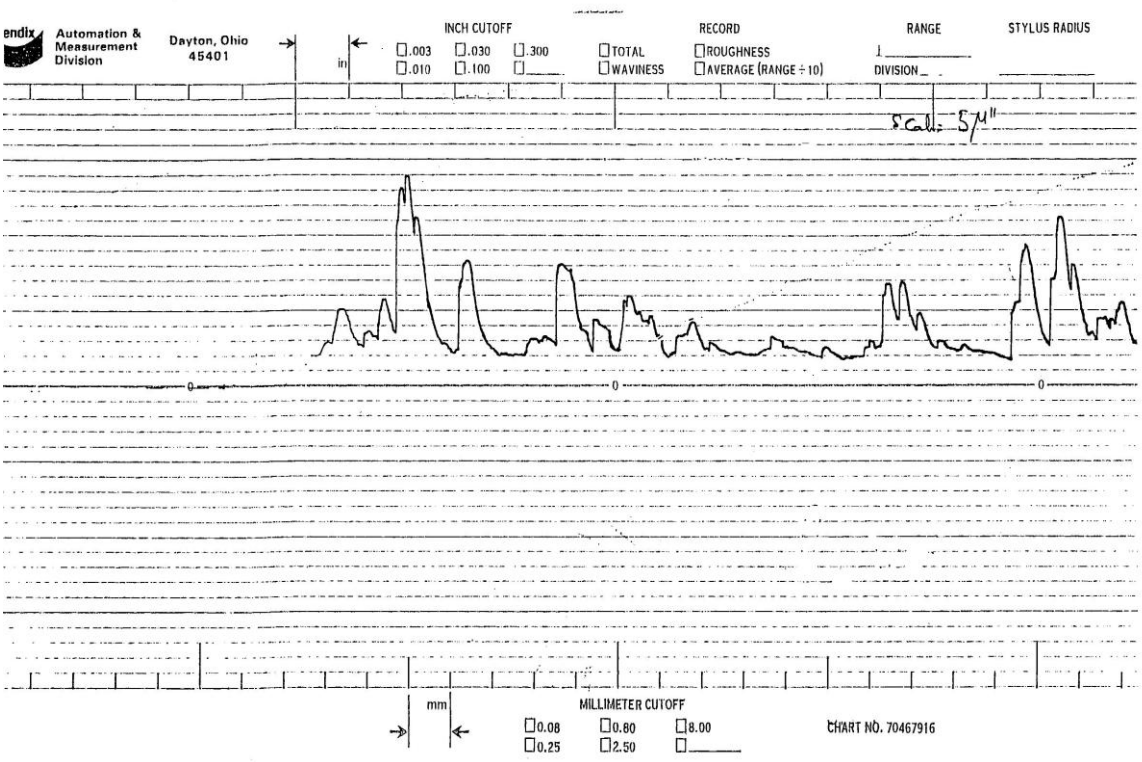

a- Forward Scan of 600-G Samples (Scale: Consecutive line spacing =5 μ")

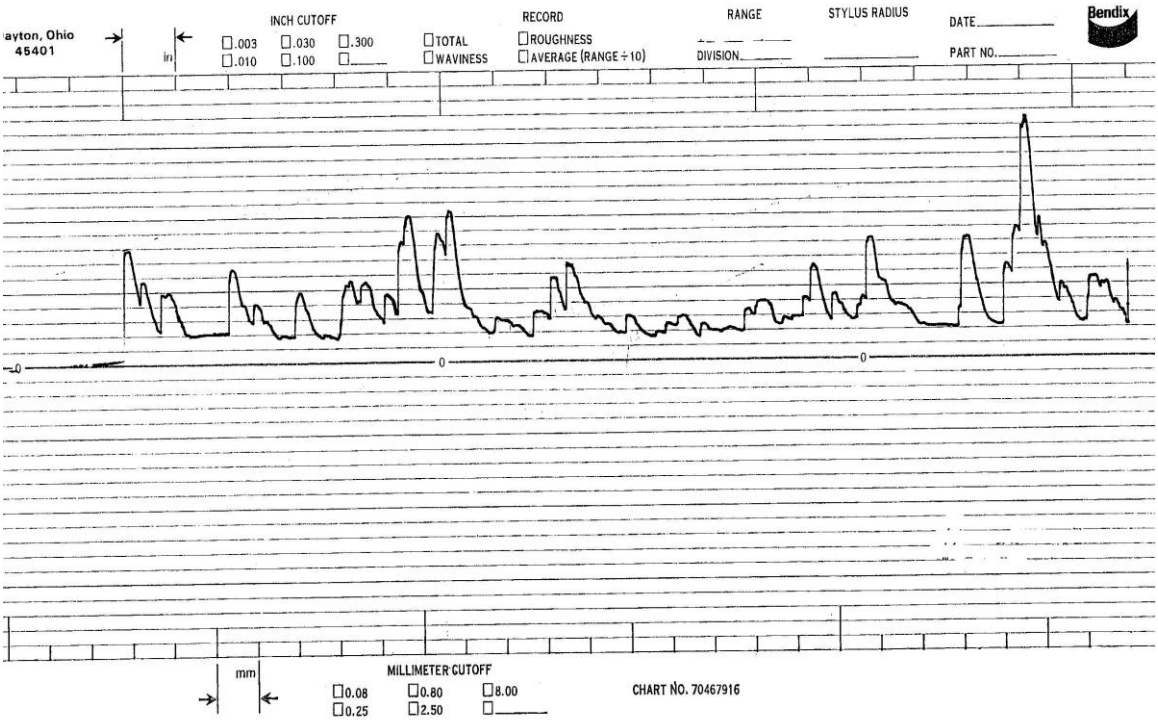

b- Reverse Scan of 600-G Samples (Scale: Consecutive line spacing =5 μ")

Figure 4.1: Surface Roughness Scans of 600-G Aluminum Sample

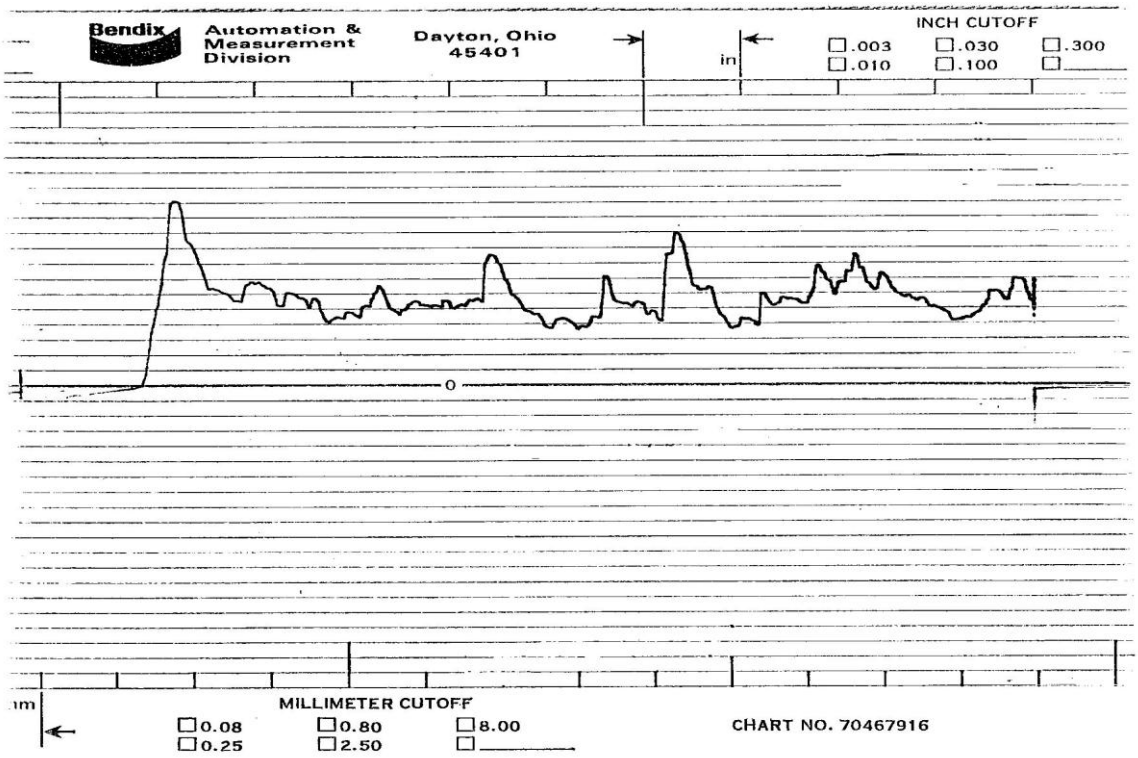

a- Forward Scan of 120-G Samples (Scale: Consecutive line spacing =10 μ")

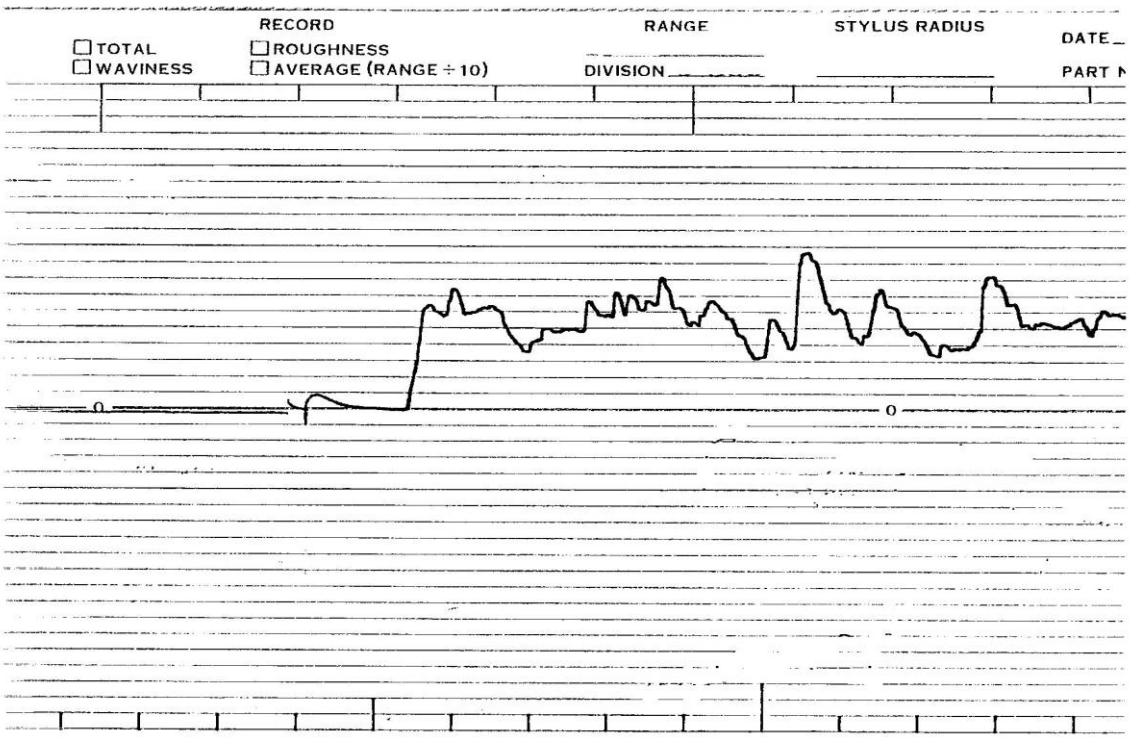

b- Reverse Scan of 120-G Samples (Scale: Consecutive line spacing =10 μ")

Figure 4.2: Surface Roughness Scans of 120-G Aluminum Sample

Table 4.1: Measured Average Surface Roughness (Ra) of 600-G & 120-G Samples

Surface Polish by SiC paper	Measurement Average Roughness Ra (µ inch)		Maximum Ra (µ inch)
	Forward	Backward	
600	70	82.5	82.5
120	120	100	120

4.2 Induction Period

The induction period for each surface polish was determined by conducting deposition experiments as a function of time at 1, 1.5, 2, 2.5 hours at fixed RPM of 500, and the same temperature and concentration stated earlier were maintained. The induction time was calculated using linear extrapolation towards time axis (x-axis) and its intercept with time axis was taken as the onset of scale deposition on the sample, i. e. the required induction time. The induction time is defined as the time between the creation of the supersaturation solution and the first observable scale on the metal surface. The results are presented in Figure 4.3. Thus the induction time determined for the 120-G samples is around 40 minutes while for the 600-G samples, it is 50 minutes. This means the scale starts to deposit on the 120-G samples just after 40 minutes from the beginning of the test, but it took 50 minutes for the 600-G samples. This behavior can be interpreted as follows. For all Aluminum samples subjected to similar hydrodynamic conditions, the rougher the surface the higher is the scale deposition they experience, and conversely the smoother the surface the less scale is attracted. Finally, the induction time depends on concentration, temperature, pH and velocity (RPM).

4.3 Solution Composition

The scale-forming solution, prepared according to the procedure outlined in Chapter 2, was analyzed by using the Ion Chromatography to determine chlorides and sulfates concentrations. Total dissolved solids (TDS) were determined gravimetrically, while the metals were determined Inductively Coupled Plasma Atomic Emission Spectroscopy.

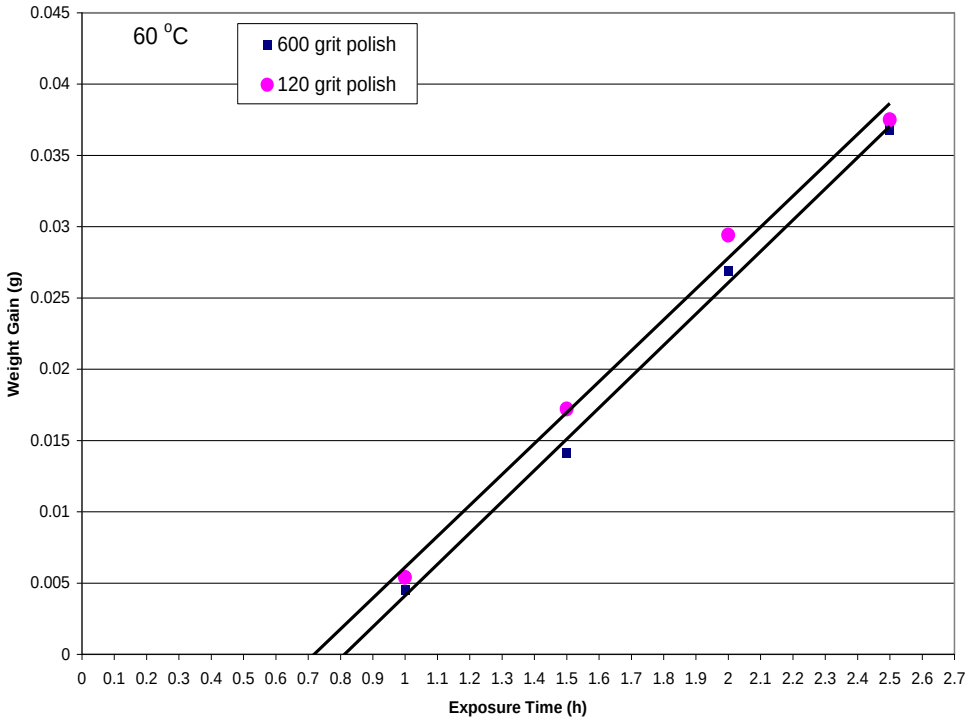

Figure 4.3: Induction Time for 120-G and 600-G Samples

The analysis of the solution composition at the inlet and exit from the test cell is given in Table 4.2. We can notice that almost constant composition of the scale-forming solution is evident from the table. Therefore, these analyses confirm that the samples were exposed to a uniform composition of the scale-forming solution throughout the duration of the experiments. The concentration of the current scale-forming solution was chosen such that no precipitation occurs at room temperature, if left un-disturbed after mixing for approximately eight hours.

4.4 Scale Deposition Studies

The speed of rotation as well as mixing of the solution had a strong influence on the rate of Calcium Sulfate scale deposition on the aluminum surface. The mass transport of the scale to the electrode surface increased as the speed of rotation increased. This process deposited a large amount of scale on the aluminum samples.

The data was analyzed out to show the effect of the solution hydrodynamics at different speeds of rotation on the rate of calcium sulfate deposition on the aluminum samples. For each rotational speed, we calculated the Reynolds number (Re) using the equation proposed by Gabe [2] as follows:

$$Re = R_1 \omega [(R_2-R_1)/\nu] \quad \textbf{(4.1)}$$

Where Re is the equivalent Reynolds number, R_1 is the radius of the rotating sample (cm), R_2 the radius of the cell (cm), ω the angular velocity of the rotating sample (rad/sec), and ν the kinematics viscosity (cm^2/s).

Table 4.2: Chemical Analysis for the $CaSO_4$ Scaling Solution at Inlet and Exit of the Test Cell

Sampling Position	Composition (ppm or mg/L)							
	Ca^{2+}	Na^{+}	Mg^{2+}	Cl^{-}	SO_4^{-2}	pH	Total Hardness	TDS
Inlet	**1010**	**1150**	**0.202**	**2150**	**2040**	**5.55**	**2520**	**6400**
Exit	**1020**	**1150**	**0.228**	**2140**	**2210**	**5.84**	**2550**	**6800**

The results presented in Table 4.3 shows the average of three measurements (triplicate test runs) that were taken at each Reynolds number for each sample. The detail of these readings is available in the Appendix A. Table 4.3 shows various Reynolds numbers and their corresponding deposition rates for the Aluminum samples that were polished with 120-G papers. The results are plotted in Figure 4.4 and 4.5, for 120-G samples. They show the deposition rate versus Reynolds number for the three sets of measurements taken, followed by the average value calculated from these measurements. It can be clearly noticed from Figure 4.5 that there is a linear relationship up to Reynolds number of 18651. This is due to the high rate of deposition which was directly proportional to the Reynolds number. Beyond this value, the deposition behavior deviated from linear increase and became horizontal. This occurred when the rate of deposition was equal to the rate of removal of scale. This means that the rate of scale deposition to the surface will not increase further and will remain constant after this value of Re.

According to the analysis carried out by Levich [27], the deposition process is diffusion controlled when the mass transfer coefficient is increased with the square root of Reynolds number, i.e. $(Re)^{0.5}$, and the Log-Log plot should give a straight line with a theoretical slope of 0.5. Therefore, the scale deposition rate on the sample surface is increasing with the rotational speed. It is obvious from the log-log plot of (D_r) vs (Re) in Figure 4.6 that a linear relationship resulted in a straight line with a slope of 0.6. This is in a close agreement with the theoretically predicted value of 0.5 by Levich although it is higher by 20%. Hence, based on our findings, we can state that the $CaSO_4$ scaling process is diffusion controlled.

Table 4.3 : Average Scale Deposition Rate for 120-G Aluminum Samples

Sr. #	Speed (rpm)	Equivalent Re	Log_{10} (Re)	D_r ($g\ m^{-2}\ h^{-1}$)	log_{10} (D_r)
1	50	746	2.873	10.291	1.012
2	100	1492	3.174	12.248	1.088
3	250	3730	3.572	20.91	1.320
4	500	7460	3.873	31.168	1.494
5	750	11190	4.049	42.51	1.628
6	1000	14921	4.174	61.678	1.790
7	1250	18651	4.271	76.966	1.886
8	1500	22381	4.350	81.996	1.914
9	1750	26111	4.417	82.576	1.917
10	2000	29841	4.475	84.143	1.925

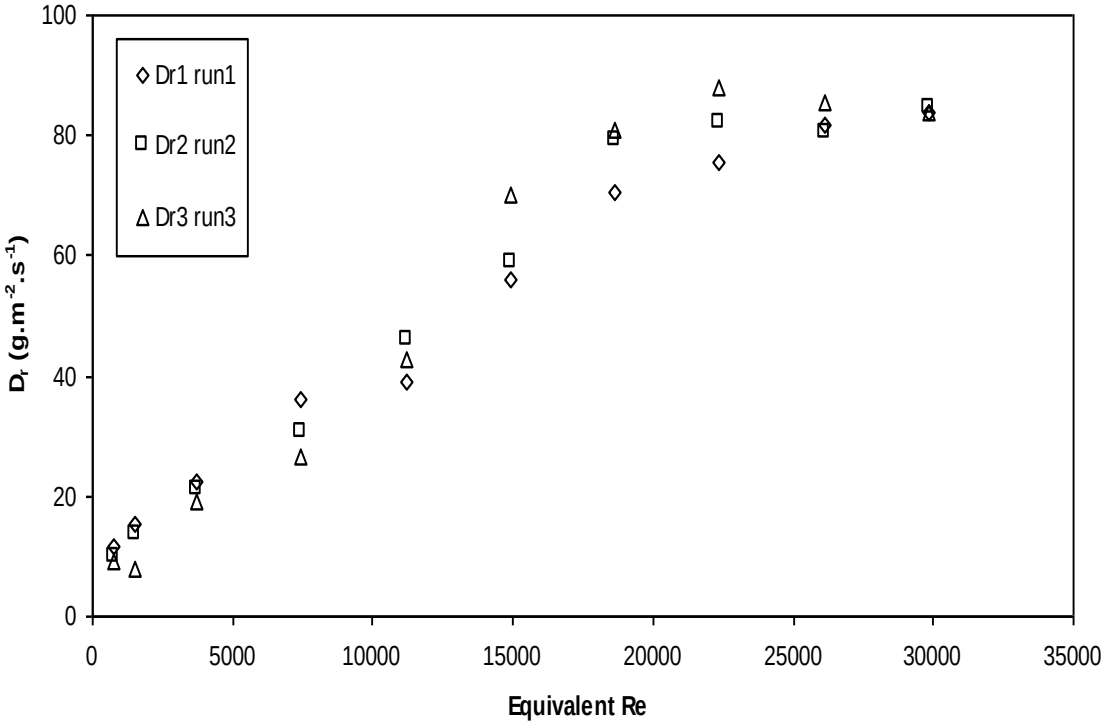

Figure 4.4: **Three Sets of Measured Data of 120-G Aluminum Samples**

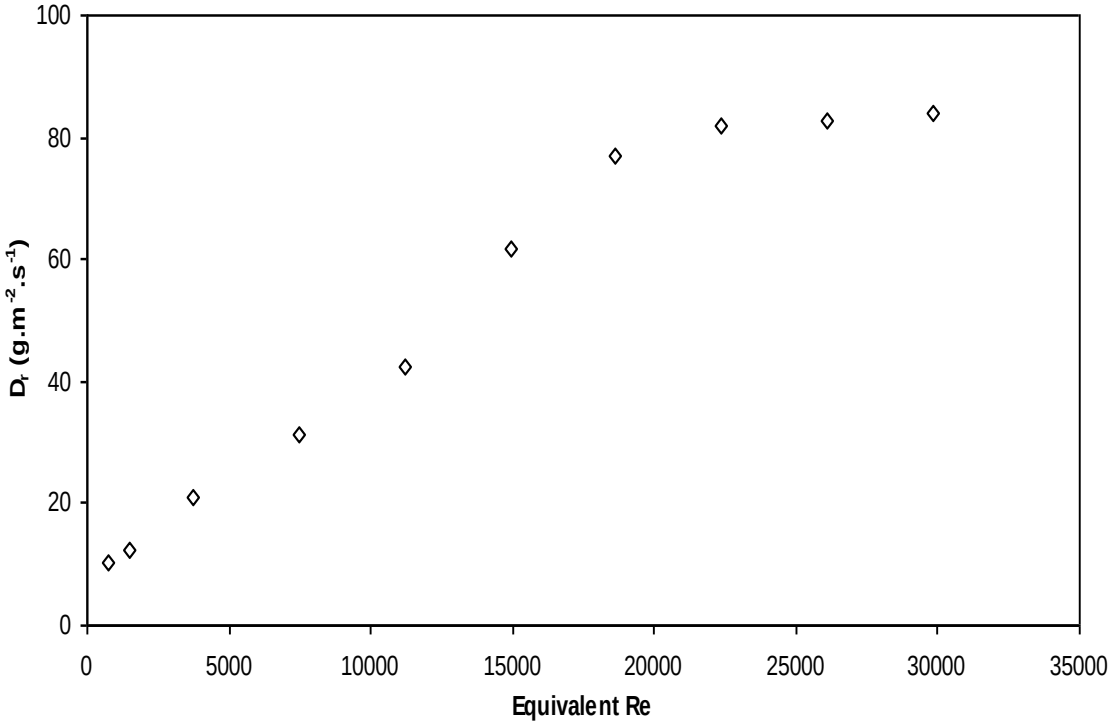

Figure 4.5: Average Deposition Rate vs. Reynolds Number (120-G)

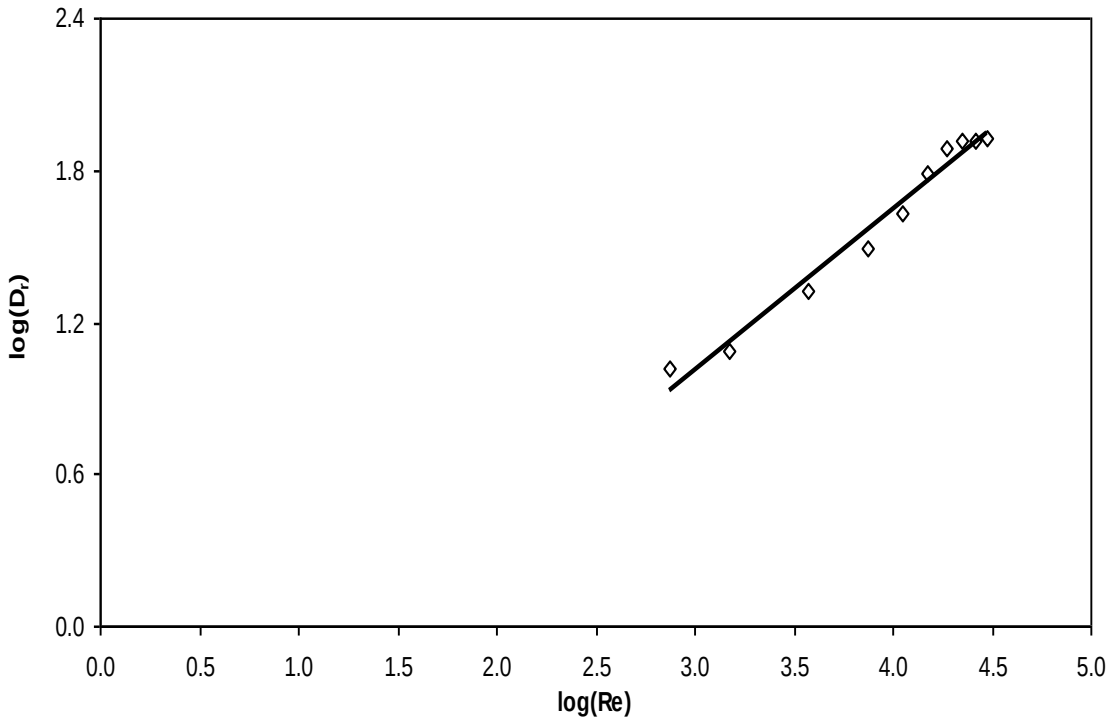

Figure 4.6: Log (Dr) vs. log (Re) of 120-G Aluminum Samples

On the other hand, the results of the deposition rate for the samples polished with 600-G (fine) paper are shown in Table 4.4. The results apparently differ from the case of the 120-G samples. An initial comparison of both tables revealed that the deposition rates for the 600-G samples are lower than for the 120-G samples. The difference ranged from 7% to a maximum of 50% which occurred at the lowest Reynolds number. Figure 4.7 presents three sets of data measurements for 600-G samples. The average of these values is plotted in Figure 4.8. The increase in deposition rate showed a linear relationship up to the Reynolds number of 15000. After Reynolds number 1000, a horizontal line resulted, due to the establishment of a balance in the rate of deposition and removal of the scale. Both 120-G and 600-G samples showed similar scaling behavior, but the horizontal line leveled off at a lower Reynolds number in the 600-G samples than in the120-G samples. In Figure 4.9 for the 600-G samples, the log-log graph of the deposition rate verses Reynolds number indicated behavior similar to the 120-G samples. The graph (Fig 4.9) showed a straight line with a slope of 0.67 for the 600-G samples. This is close to the theoretical value of 0.5 [27] with a deviation of 34 %.

4.5 Comparison of $CaSO_4$ on Aluminum and Stainless Steel 316

In the following test we present a comparison of $CaSO_4$ scale deposition on Aluminum and Stainless Steel surfaces obtained from the current study and earlier results from literature on Stainless Steel 316 [8]. The samples of both materials were polished with 600-G (identical preparation). In both cases the samples were

Table 4.4: Scale Deposition Rate for 600-G Aluminum Samples

Sr. #	Speed (rpm)	Equivalent Re	$\log_{10}$ (Re)	D_r (g m^{-2} h^{-1})	Log_{10} (D_r)
1	50	746	2.873	4.800	0.6812
2	100	1492	3.174	8.778	0.9434
3	250	3730	3.572	11.622	1.0653
4	500	7460	3.873	23.672	1.3742
5	750	11190	4.049	39.749	1.5993
6	1000	14921	4.174	56.187	1.7496
7	1250	18651	4.271	58.259	1.7654
8	1500	22381	4.350	58.949	1.7705
9	1750	26111	4.417	59.837	1.777
10	2000	29841	4.475	60.527	1.7819

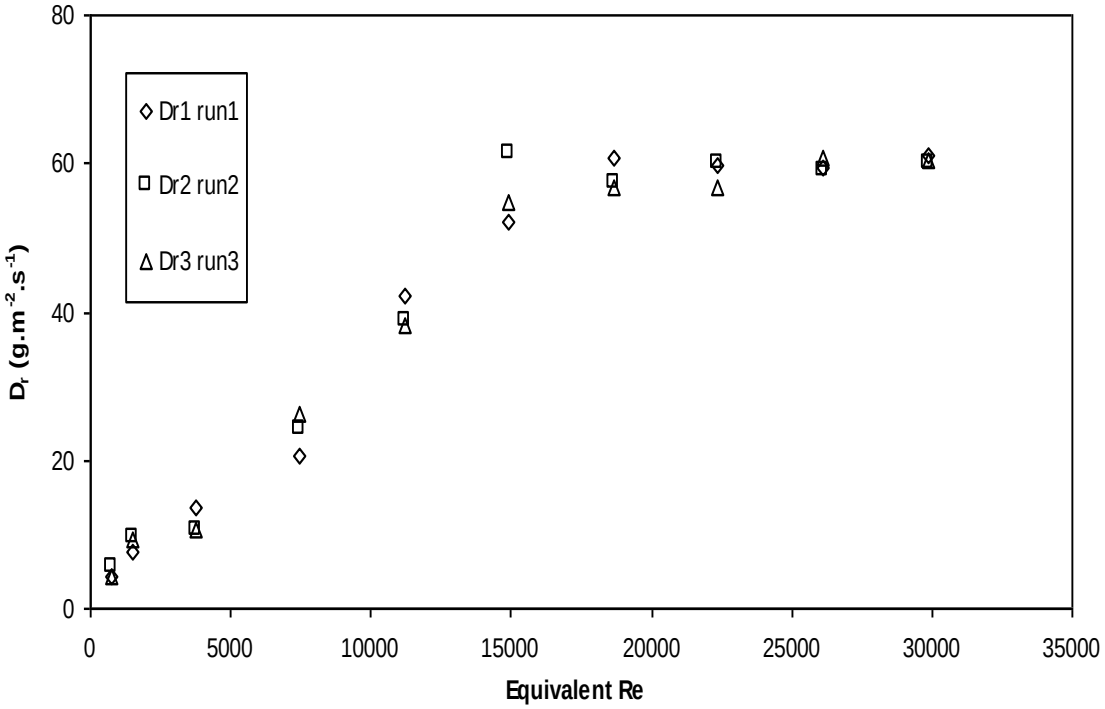

Figure 4.7: Three Sets of Measured Data of 600-G Aluminum Samples

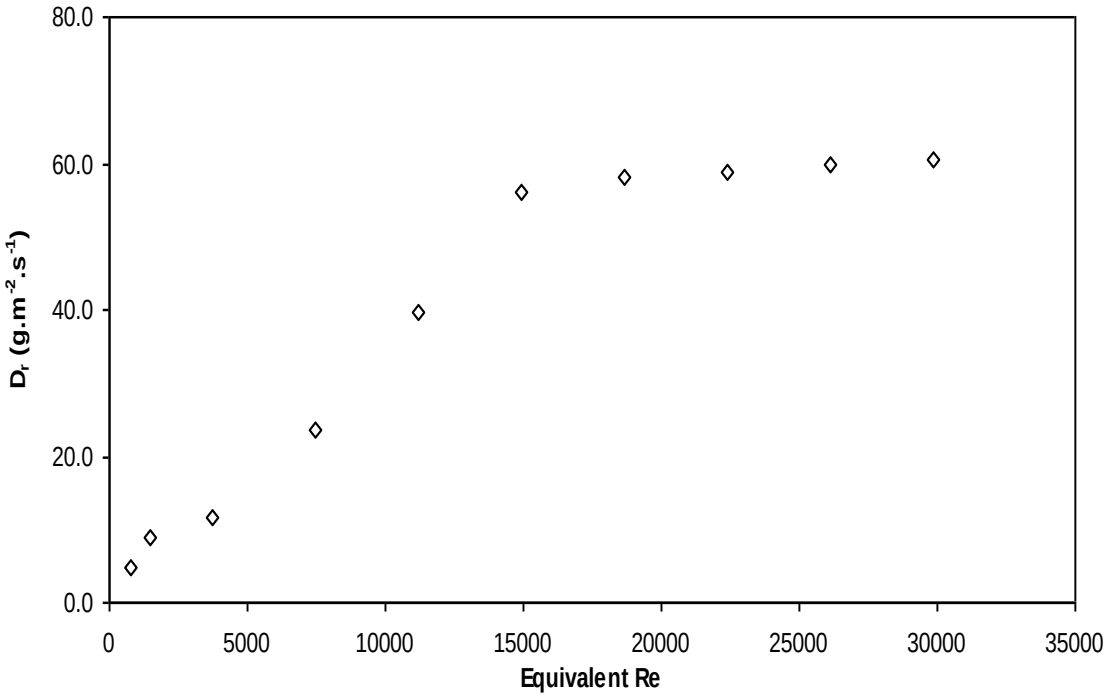

Figure 4.8: Average Deposition Rate vs. Reynolds Number (600-G)

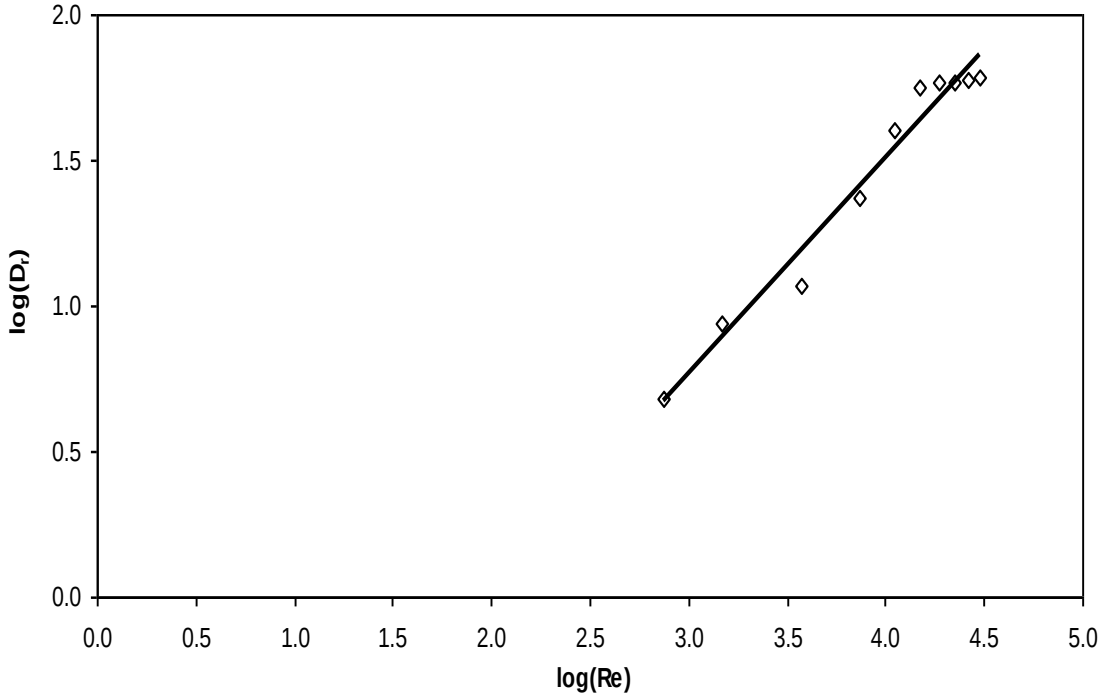

Figure 4.9: Log (D_r) vs. Log (Re) of 600-G Aluminum Samples

subjected to the same solution concentration, temperature and duration of the test (identical test conditions).

In Table 4.5 we present a comparison between the deposition rates of Calcium Sulfate $CaSO_4$ scale on the aluminum and stainless steel SS-316 samples, both polished with 600-grit size. For the first four Reynolds numbers (i.e. Re 746 to 7460), the deposition rate on the Aluminum samples was lower, which means less scale attached to their surfaces. These four values of Reynolds number fell within the linear relationship range between the deposition rate and Reynolds number.

As the Reynolds number increased from 7460, the Aluminum samples gained more scale deposition than the stainless steel. This occurred mainly above the Reynolds number of 11000 as shown in Figure 4.10. We can state that, if we have the option to choose between the two metals subjected to similar test conditions, the Aluminum material is recommended when the flow has a Reynolds number lower that 11000, but otherwise the Stainless Steel 316 will be preferable.

4.6 Photographs of Scale Deposition for 120-G and 600-G Aluminum Samples

In the following section, we will show and discuss the scale behavior for a number of selective samples polished with 120 and 600 grit sizes respectively. The following photographs show the Calcium Sulfate $CaSO_4$ deposition obtained on Aluminum metal surface at different Reynolds numbers in the present study.

120-G Samples: Figure 4.11 shows the scale deposition at Reynolds number 746 for 120-G samples. The scale is uniformly distributed over the entire surface, but it appears spongy and it is not firmly adhering to the surfaces. At this Reynolds numb-

Table 4.5: Comparison of Deposition Rate Between Aluminum and Stainless Steel-316

Sr. #	Equivalent Re	D_r(Al) (g m^{-2} h^{-1})	D_r (SS) (g m^{-2} h^{-1})	Difference D_r (D_{ss}-D_{Al})
1	746	4.800	7.430	+ 2.630
2	1492	8.778	12.250	+ 3.472
3	3730	11.622	15.890	+ 4.268
4	7460	23.672	26.360	+ 2.688
5	11190	39.749	34.030	- 5.719
6	14921	56.187	37.870	- 18.317
7	22381	58.949	41.850	- 17.099
8	29841	60.527	52.040	- 8.487

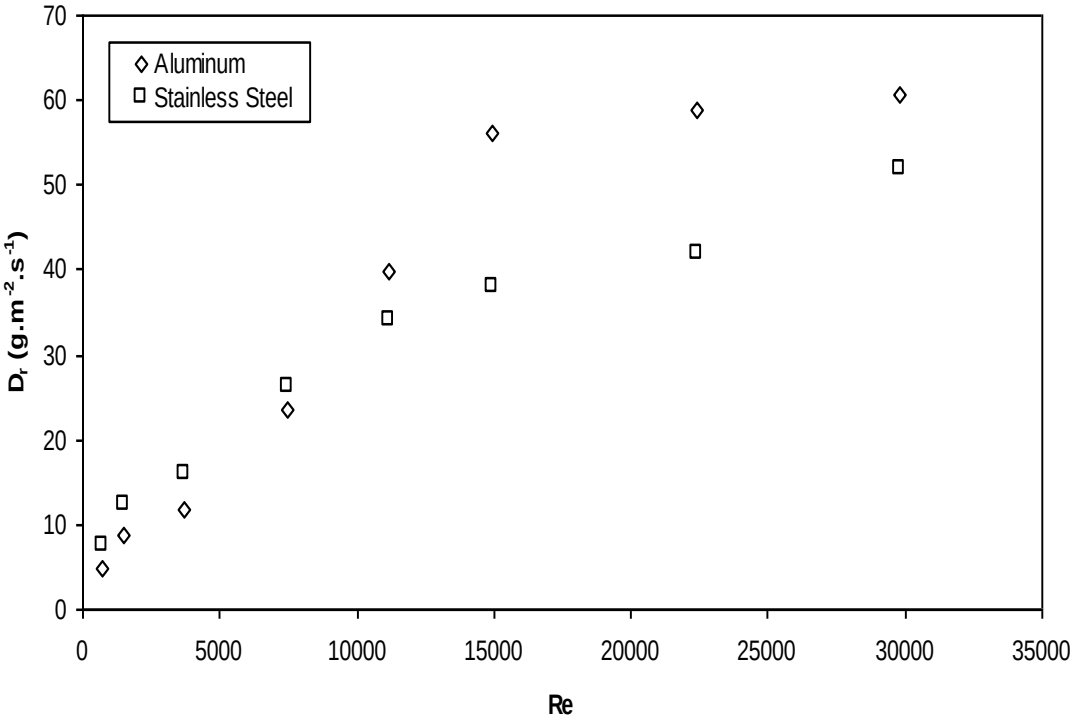

Figure 4.10: Aluminum vs Stainless Steel Deposition Rate Comparison for 600-G

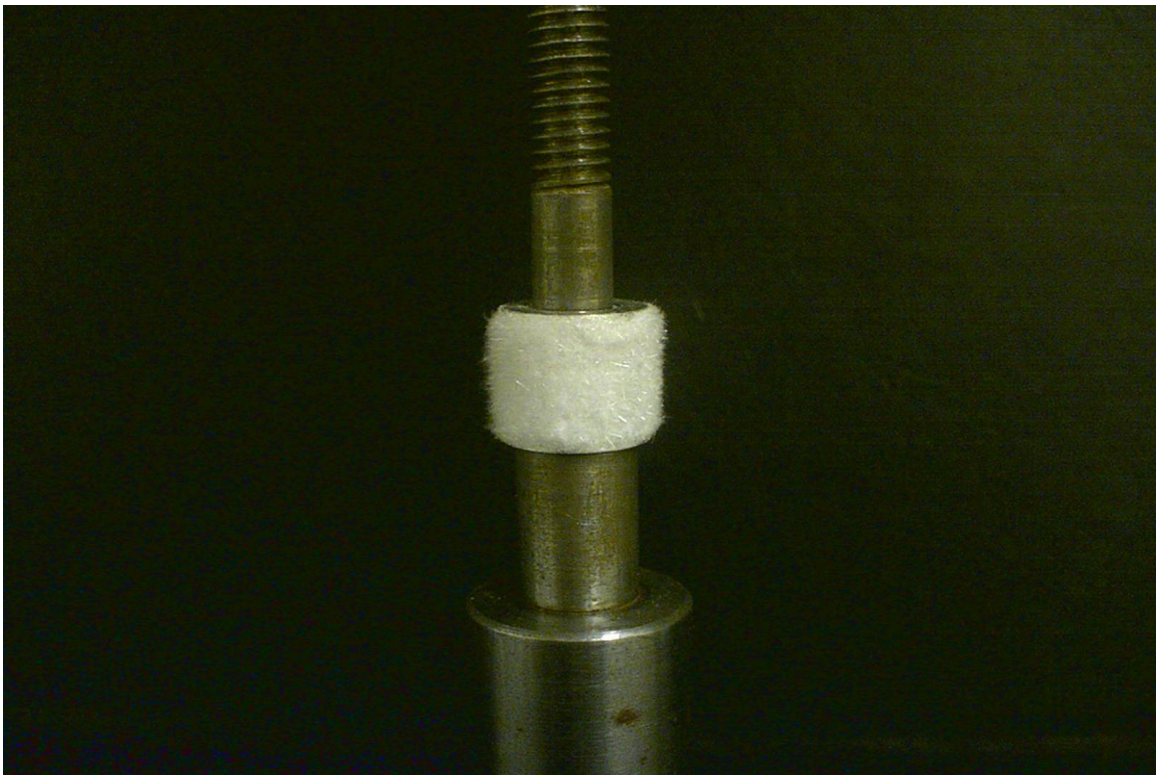

Figure 4.11: Photograph of Scale Deposition at Reynolds Number of Re=746, 120-G

er, the flow regime is laminar. As the Reynolds number increases to 1492, the scale pattern changes from the previous uniform distribution to a scattering, due to the flow regime change that disturbs the uniform pattern with more scale deposition on some locations than others, as shown in Figure 4.12. The scale at this stage is more compact at the sample surface, which led to extra weight gain than occurred at the lower Reynolds numbers.

Now, moving to a higher Reynolds number of 7460 as shown in Figure 4.13, the weight gained by the sample is higher than in the case of Reynolds number of 1492, the scale deposition pattern is irregular and more compact especially at the edges of the sample. At this value of Reynolds number the rate of deposition is higher than the rate of removal which justifies the higher weight gained this time.

The scale deposition pattern changed significantly for the Reynolds number of 11190 as shown in Figure 4.14. In this case, there is minor scale build-up in the middle of the sample, and scale is deposited only on its upper and lower ends. Also the scale is dense and compact, and the weight gain is almost 50% more than in the case of Re of 7460.

For the Reynolds number of 22381, there is clearly no scale deposition at the middle of the sample because the rate of removal supersedes the rate of deposition at the middle of the sample as shown in Figure 4.15. However, scale formed only at the upper and lower ends of the sample. The scale on both ends is dense and compact as was in previous figure but with more weight gained than in the previous case.

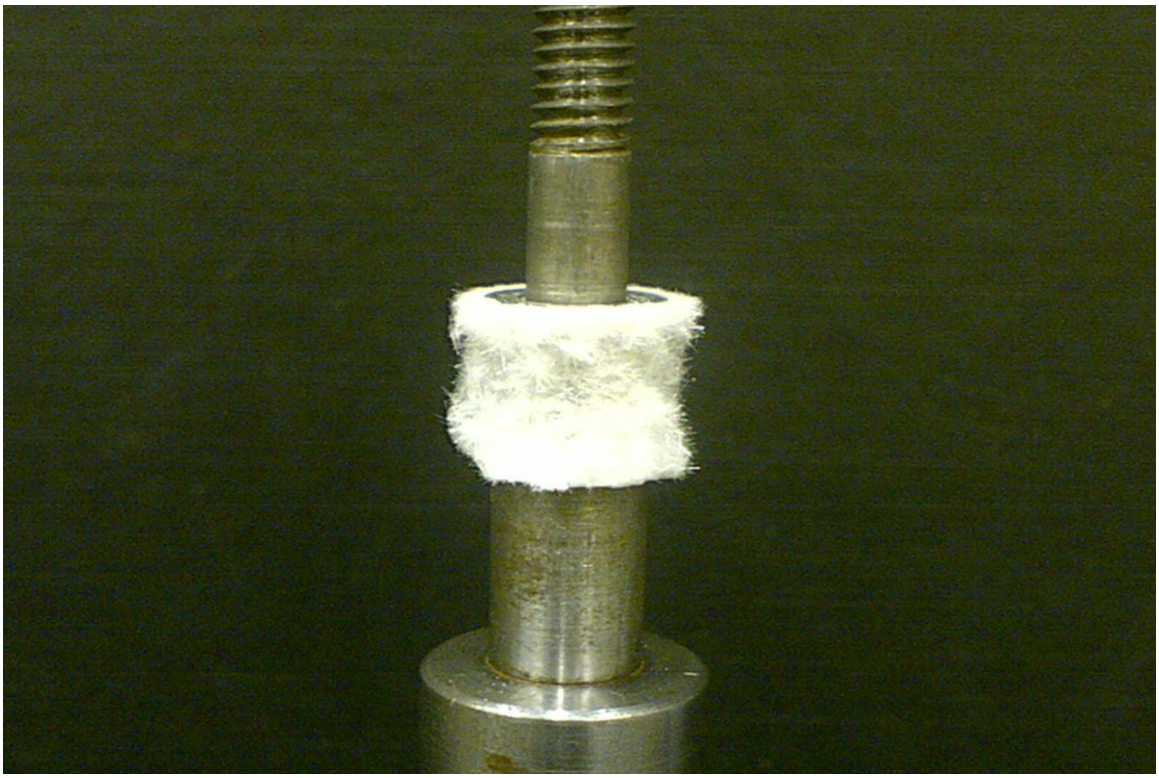

Figure 4.12: Photograph of Scale Deposition at Reynolds Number of Re=1492, 120-G

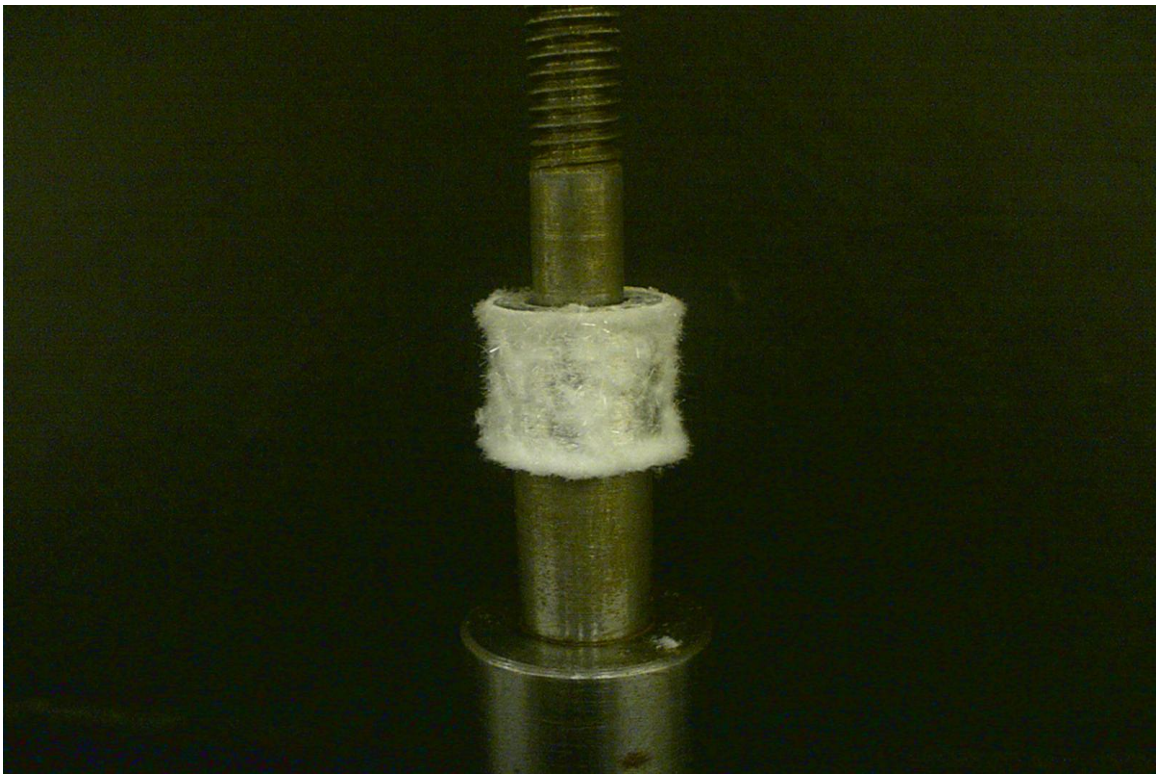

Figure 4.13: Photograph of Scale Deposition at Reynolds Number of Re=7460, 120-G

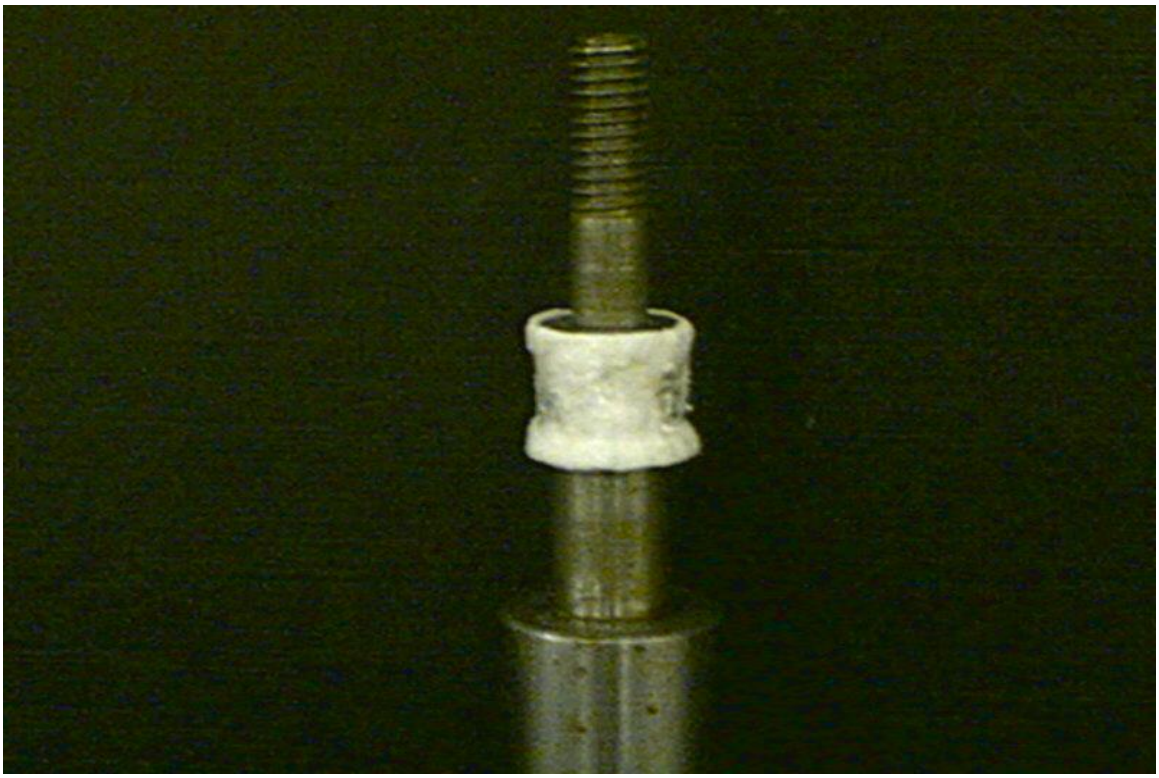

Figure 4.14: Photograph of Scale Deposition at Reynolds Number of Re=11190, 120- G

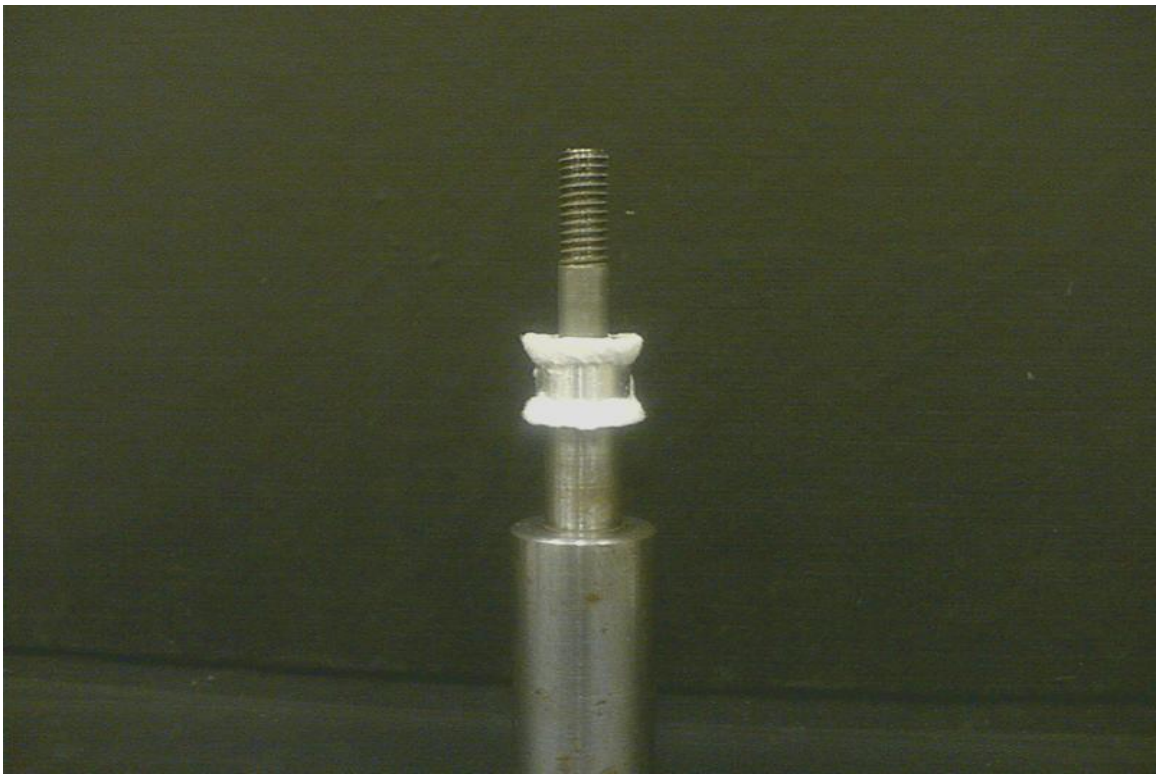

Figure 4.15: Photograph of Scale Deposition at Reynolds Number of Re=22381, 120-G

600 Grit Samples: Figure 4.16 to 4.18 show typical results of scale deposition on the Aluminum metal surface polished with 600 grit size. These photographs represent the Reynolds numbers of 746, 7460 and 22381 respectively. On the 600-G samples, the behavior was very similar to that we saw earlier on the 120-G surfaces. The main difference was in the weight gain, which was higher for the case of the 120-G than for the 600-G samples tested at the same Reynolds numbers. For example, the scale pattern in Figure 4.16 (the 600-G Aluminum surface at Reynolds number 746) was similar to Figure 4.11 for the 120-G. The weight gain as shown in Table 4.6 , was higher by 50% for the 120-G samples than for the 600-G sample at identical Reynolds numbers.

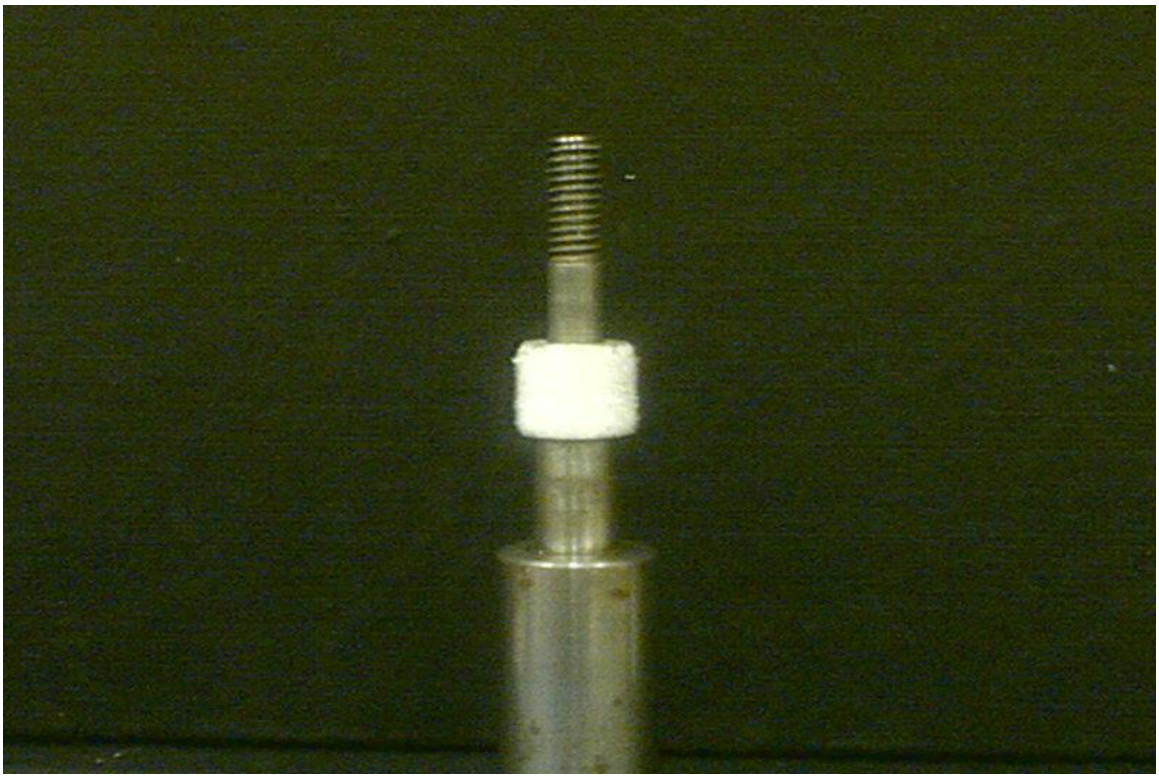

Figure 4.16: Photograph of Scale Deposition at Reynolds Number of Re=746, 600-Gt

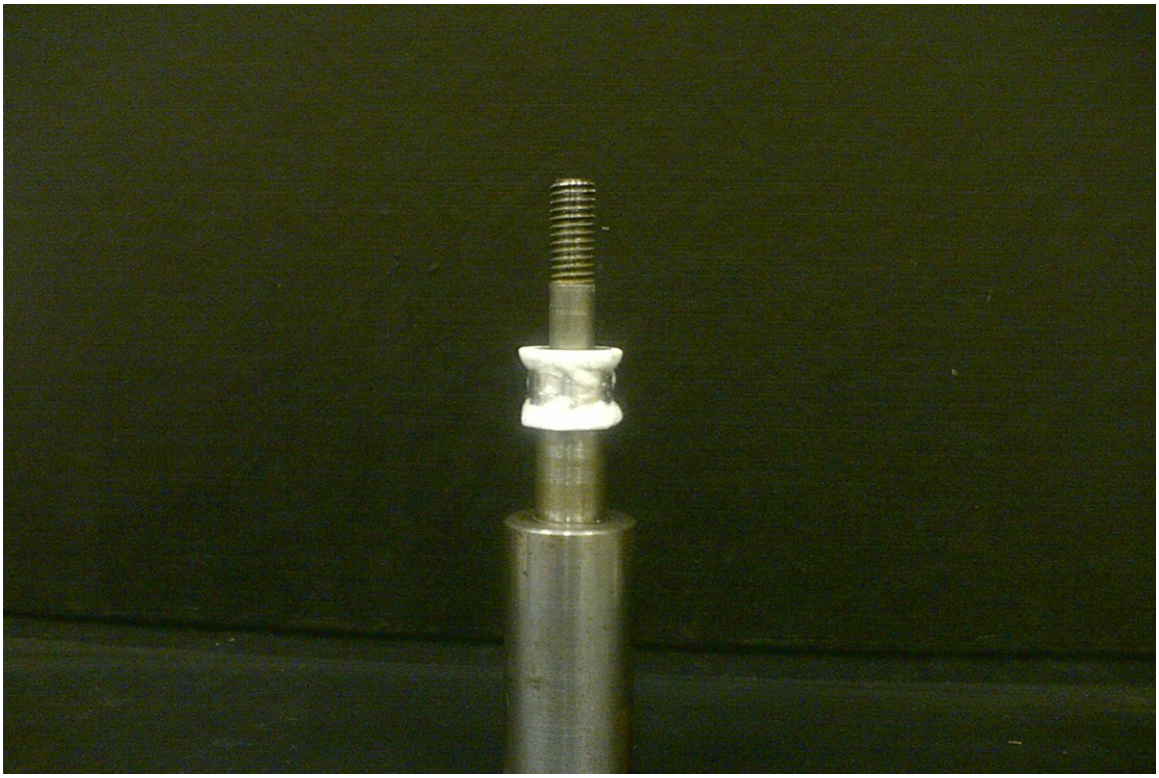

Figure 4.17: Photograph of Scale Deposition at Reynolds Number of Re=7460, 600-G

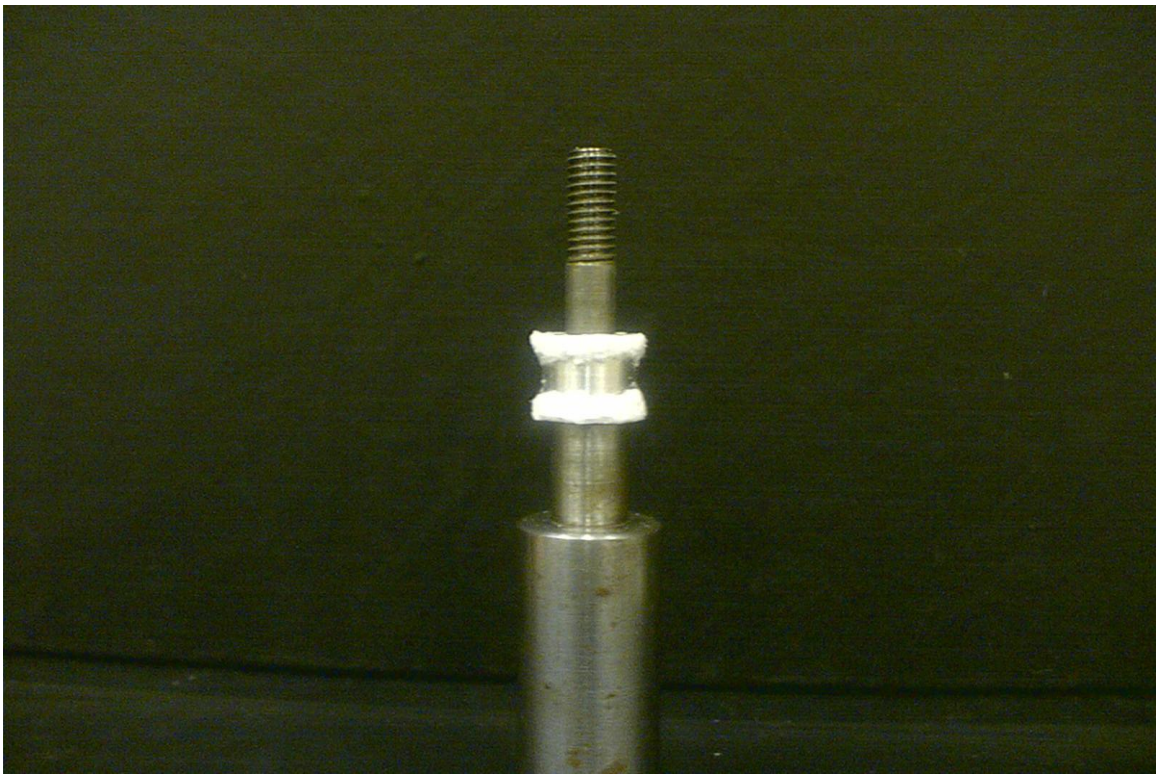

Figure 4.18: Photograph of Scale Deposition at Reynolds Number of Re=22381, 600-G

In Table 4.6 , we illustrate a comparison between the average deposition rates of the samples polished with 120 & 600 grit sizes. In all cases, the deposition rate with 120-grit size is higher than for the 600 size. The percentage difference ranged from 6.5% at Re 11190 to 50% at Re 746. Moreover, upon reaching the constant deposition rate at the last three Reynolds numbers, the difference in the deposition rates was also constant at 28%.

Several points are thus clarified. The rate of deposition increases as the Reynolds number is increased, and so the mass transfer increases since more scale is deposited on the metal surface as the speed of rotation increases. The log-log plot of the deposition rate versus the Reynolds number gives a slope close to 0.5 for Aluminum samples of both 120-G and 600-G. The process is diffusion controlled; and this point agrees with the observation by Quddus and Allam [8] for the Barium Sulfate scale and for the Calcium Sulfate scale [10] on Stainless Steel-316. As the speed of rotation increased, the scale deposition on the metal surface became harder and stiffer and more compact an with increase in the weight gain on the metal surface.

Table 4.6: Comparison of Average Deposition Rate of Al Samples for 120-G & 600-G Samples

Sr. #	Speed (rpm)	Equivalent Re	120 grit D_r ($g\ m^{-2}\ h^{-1}$)	600 grit D_r ($g\ m^{-2}\ h^{-1}$)	Difference ($g\ m^{-2}\ h^{-1}$)
1	50	746	10.291	4.800	5.491
2	100	1492	12.248	8.778	3.47
3	250	3730	20.91	11.622	9.288
4	500	7460	31.168	23.672	7.496
5	750	11190	42.51	39.749	2.761
6	1000	14921	61.678	56.187	5.491
7	1250	18651	76.966	58.259	18.707
8	1500	22381	81.996	58.949	23.047
9	1750	26111	82.576	59.837	22.739
10	2000	29841	84.143	60.527	23.616

Morphological Study of $CaSO_4$ Scale

5.1 Scale Morphology

The SEM examination revealed various crystal structures comprising prismatic rods and needles-like growth. At some location plates similar growth was noticed. Generally the $CaSO_4$ crystals initially tend to grow perpendicular to the substrate surface and then branch out randomly in all directions. This feature among others is perhaps a typical characteristic of the $CaSO_4$ crystal growth mechanism. This feature was also observed earlier by Quddus [10] when he studied the $CaSO_4$ deposition on Stainless Steel.

The micrograph in Figure 5.1 shows the general morphology exhibited by an Aluminum surface when exposed to a solution containing $CaSO_4$ scale species. It clearly depicts the presence of a dense population of uniformly distributed $CaSO_4$ crystals on the entire surface of the substrate, but some locations have more scales than others. Similar results were noticed in earlier studies for $BaSO_4$ [8], $SrSO_4$ [9], and $CaSO_4$ [10] scale formation on stainless steel-316 surfaces.

The micrographs of Figure 5.2 and Figure 5.3 reveal the prismatic rods and needles successively emanating from the already deposited primary crystals. Also, these micrographs show the perpendicular growth of $CaSO_4$, which appears to be a pertinent mechanistic feature of $CaSO_4$ scale formation.

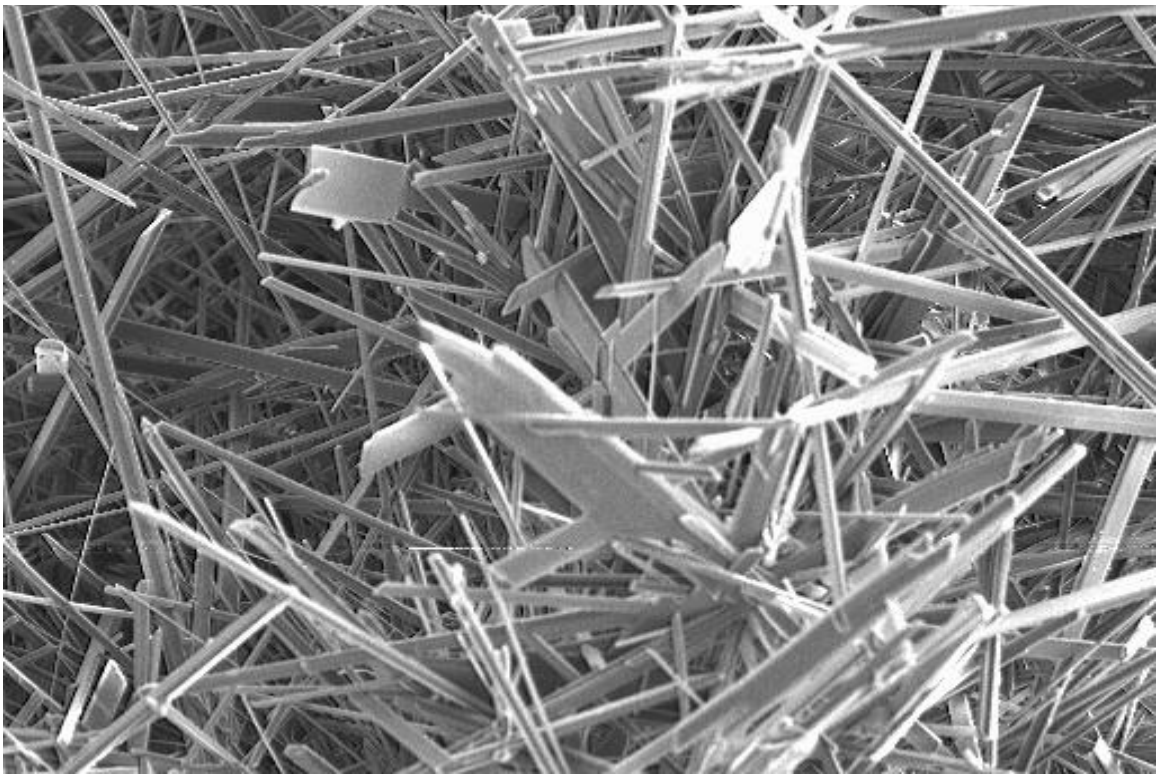

Figure 5.1: General Morphology of $CaSO_4$ on Aluminum Metal Surface (120-G)

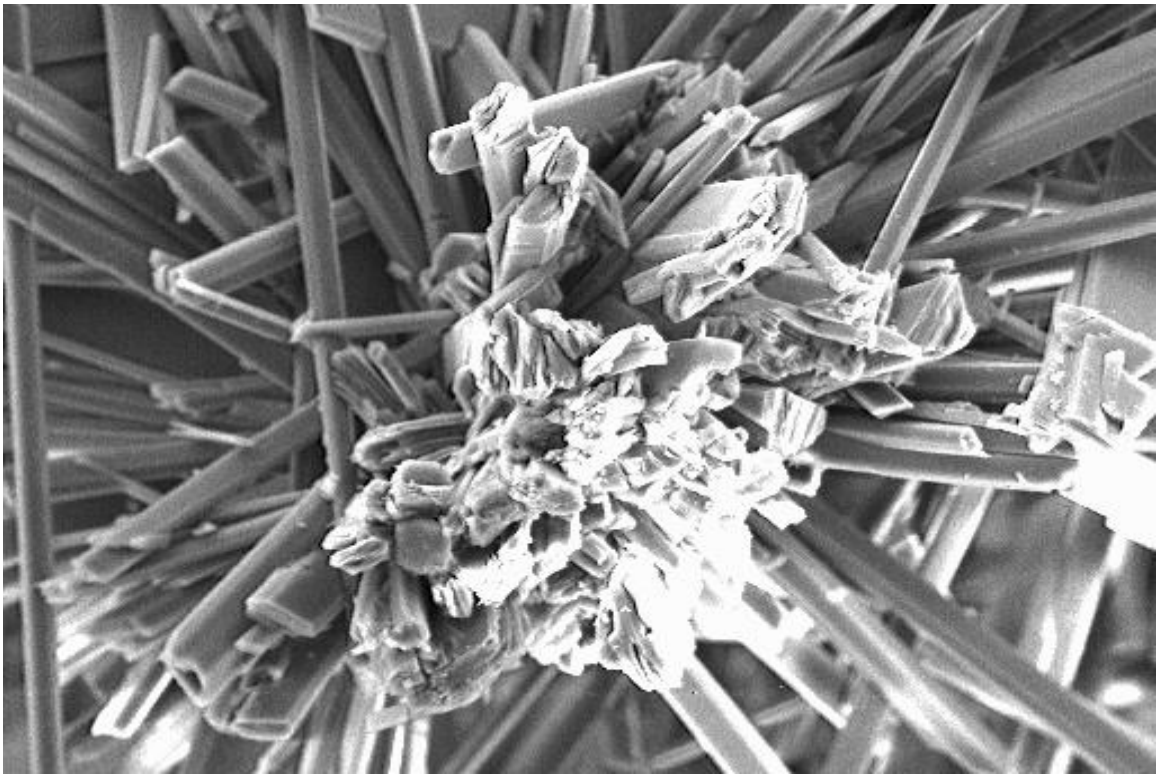

Figure 5.2: Prismatic Rods for 120-G Aluminum Surface

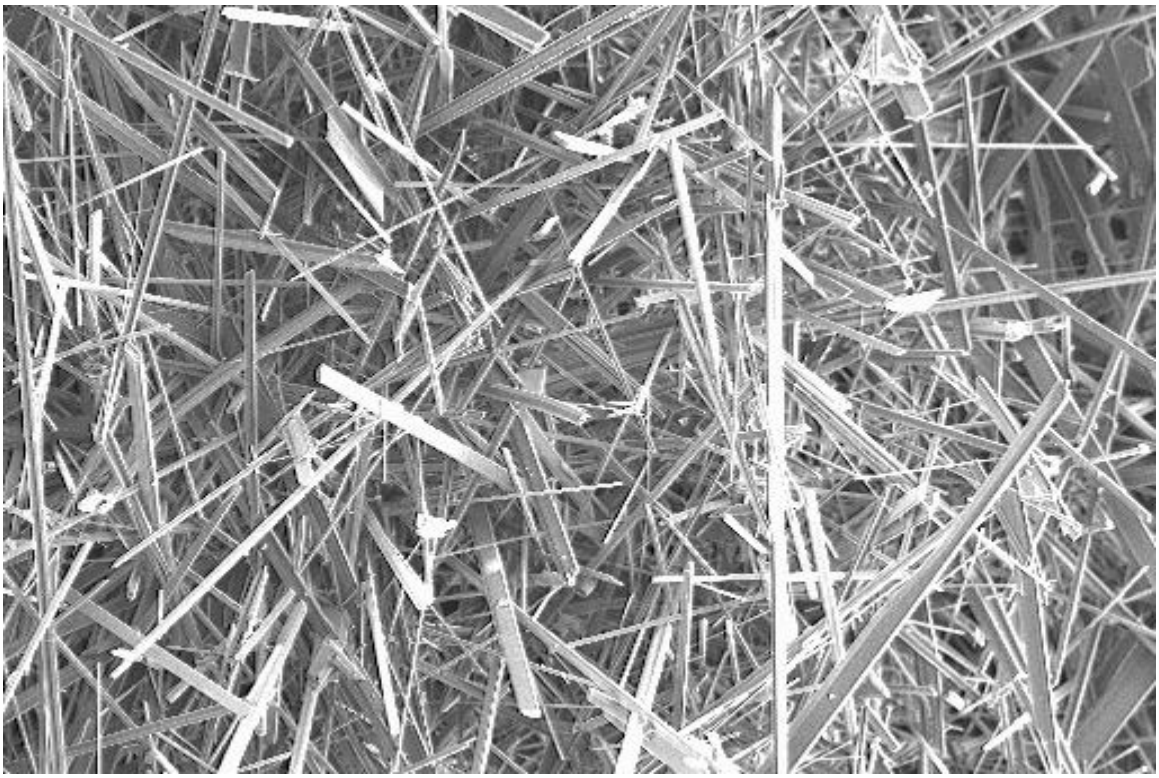

Figure 5.3: Needles Formation for 600-G Aluminum Surface

It is envisaged that, once a thin layer of scale is formed, the subsequent scale growth will be faster because of the readily available abundant nucleation sites as compared to the base polished surface. Another perception may be that the scaled surface becomes sufficiently rough to develop a larger surface area which promotes more deposition than does the original polished surface.

Both 120-G and 600-G samples had almost the same scale morphology. This same scale morphology was exhibited by earlier studies by Quddus [10] for Stainless Steel 316. The 600-G samples showed thinner needles than the scale on the 120-G surfaces, and we attributed this to the surface roughness which was lower in the 600-grit polish paper than the 120. Finally, morphology or crystals growth habit does not vary much in general except due to certain special unknown reasons.

CONCLUSIONS AND RECOMMENDATIONS

6.1 Conclusions

Based on the results of the present experimental study, the following conclusions can be made:

1. The data analysis of the $CaSO_4$ scale deposition rate shows that rotational speed and mixing the scale-forming solution have a strong influence on the rate of Calcium Sulfate deposition on the Aluminum surface. The higher the speed of rotation, the more scale crystals adhered to the metal surface. The deposition rate increased linearly with almost the square root of the Reynolds number, which showed that the process is diffusion controlled. For both 120-G and 600-G samples, the deposition rate has a clear linear relationship with the speed of rotation before approaching a steady condition of leveling off. After that, the relationship between Reynolds and deposition rate showed a straight line with a slope of almost zero. The point of leveling off was higher for the 120-G samples than 600-G.

2. The deposition rate for the 600-G surfaces was lower than for the 120-G; i.e. it ranged from 53% to almost 6.5%. This resulted from the surface roughness profile, i.e. the more polished 600-G surfaces revealed less scale deposition compared to the rough 120-G surfaces.

3. The present experiment shows that the scale build-up on the Aluminum surface is directly proportional with the rotational speed. As the speed increases, the deposition rate increases, resulting in more weight gained by the surface. For low speed, the

deposited scales look spongy, loose and less adherent to the surface. However, as the speed increases, the scales get more attached and compact on the metal surface.

4. SEM analyses indicated that the scale morphology structure contains prismatic rods and needle-like crystal growths. At some locations, a plate-like growth was noticed. Generally the $CaSO_4$ crystals initially grew perpendicular to the metal surface and then branched out randomly. This feature specifically was observed earlier by Quddus [10] when he studied the effect of $CaSO_4$ on SS-316 metal surface. The distribution of the $CaSO_4$ crystals on the Aluminum surface was uniform at low Reynolds numbers. Once a thin layer of scale is formed, the subsequent scale layer growth on it occurs much faster because of the readily available abundant nucleation sites compared to the initially polished surface. Another perception may be that the scaled surface becomes sufficiently rough to promote deposition process faster than does the bare surface. Both 120-G and 600-G surfaces have almost the same scale morphology, except that for the 120-G surface the needle crystals were thicker than for the 600-G surfaces.

5. By comparing the deposition rate for the 600-G samples with the earlier study of Stainless Steel [10] under the same test condition, the scale deposition rate on Aluminum was lower than the Stainless Steel 316 when the Reynolds numbers are below 7460. However, Aluminum showed more scale than Stainless Steel, which occurred above Reynolds 11000 in the present study. We conjecture that the surface roughness of the two materials were not exactly the same, although they were polished with the same grit size paper. Aluminum is softer than Stainless Steel, and therefore it has a coarser surface texture compared to Stainless Steel when polished with same grit paper.

6. The uncertainty analysis was conducted for the measured variables such as: diameter (D), Length (L), Duration of the test (t) and Weight gained (W_g) by the sample after

each test run in our experimental work for all deposition rate measurements. This analysis showed that the results for the 120-G samples had a percentage error ranging from 2% to 3%, while for the 600-G samples it varied from 2.6% to 4.5%. The sensitivity of the resulting error in weight gained was greater at low rotational speed than at the middle and high speeds. However, the diameter and length showed the opposite error, with low sensitivity at low speed of rotation and greater sensitivity as the speed increases. For all the tests, the measured duration has a negligible and constant effect on the error, at either low or high Reynolds numbers.

7. Finally, from the uncertainty analysis for all Reynolds numbers as shown in Appendix-A, we found that viscosity is the main parameter contributing to the resulting error. That is why we held the test at constant temperature because of the sensitivity of viscosity to temperature variation, which could affect our result greatly if it was not controlled. The other parameters contributing to the error like sample (R_1) and the cell (R_2) added error to the results, but with more influence from the cell radius since it impacts the shear stress more than the sample radius. The rotating speed influenced the error only at the low Reynolds number. However, for the intermediate and high Reynolds numbers, it made a negligible contribution to the resulting error.

6.2 Recommendations

Following are our recommendations for the future study:

1. The present experiment work can be extended to study different materials used in the field for heat transfer equipment, such as coated carbon steel, copper and different grades of Stainless Steel rather than Stainless Steel 316. Also, further analyses can be done by investigating the combined effect of different salts using sea water to simulate the real situation found in desalination plants.

2. The present work can be extended for Reynolds numbers not yet covered.

3. The present study can be extended for different surface roughness, as other than the 120 & 600 grit size.

4. The present study can be extended for temperatures other than 60 C^{o}.

Nomenclature

A_s Clean surface area for the sample (m^2)

Al Aluminum

D Diameter of the sample (m)

D_r Scale Deposition rate ($g\ m^{-2}\ h^{-1}$)

ESD Energy Dispersive Spectrometer

L Length of the sample (m)

M Molar concentration

PAA Polyacrylic acid

R_1 Outer radius of the sample (cm)

R_2 Inner radius of the test cell (cm)

t Duration time of each test run measured in hour (h)

V Tangential Linear velocity (m/s)

W_g Weight gained by the sample after each test run (g)

Re Reynolds number, $Re=R_1\ \omega\ [(R_2-R_1)/\nu]$

ΔT Change in temperature measured in (°C)

Greek Symbols

ν = Kinematics viscosity of the solution ($cm^2\ .s^{-1}$)

ω = Angular velocity (rad/s)

ρ = density of the solution (g/cm^3)

References

[1] Silverman D.C. “Rotating Cylinder Electrode – Geometry Relationships for Prediction of Velocity-Sensitive Corrosion”, Corrosion, Vol. 44, pp.42-49 (1988).

[2] Gabe D. R. "The Rotating Cylinder Electrode", Journal of Applied Electrochemistry, Vol. 4, pp.91-108 (1974).

[3] Steinhagen H. M. "Fouling of heat exchanger surfaces", Chemistry & Industry, Vol. 50, March 6 (1995).

[4] Neusen K. F., Chan S. H. and Zhou D. Z "Heat transfer in Geophysical and Geothermal Systems", Vol. 76, pp. 45-50. ASME HTD, New York, 1987.

[5] Gudmundson J. S. "Particulate Fouling", Fouling of Heat Transfer Equipment, pp. 357-387. Hemisphere Publishing Compant, Washington D. C., 1981.

[6] Neville A., Hodgkiess T. and Morizot A. P. "Electrochemical assessment of calcium carbonate deposition using a rotating disc electrode (RDE)", Journal of Applied Electrochemistry, Vol. 29, pp. 455-462 (1999).

[7] Chen T., Neville A. and Yuan M. "Calcium carbonate scale formation-assessing the initial stages of precipitation and deposition", Journal of Petroleum Science & Engineering, Vol. 46, pp.185-194 (2005).

[8] Quddus A. and Allam I. M. "$BaSO_4$ scale deposition on stainless steel" Desalination, Vol. 127, pp. 219-224 (2000).

[9] Khokhar M. I., Somuah S., Amabeoku M., Allam I. M. and Quddus A. "Oilfield scaling: mechanism of formation" Proc. 4th Middle East Corrosion Conference, Bahrain, Vol. 1, pp. 244-258 (1998).

[10] Quddus A. "Effect of hydrodynamics on the deposition of $CaSO_4$ on stainless steel" Desalination, Vol. 142, pp. 57-63 (2002).

[11] Neville A., Morizot A. P. "Calcareous scales formed by cathodic protection –an assessment of characteristic and kinetics", Journal of Crystal Growth, Vol. 243, pp. 490-502 (2002).

[12] Morizot A. P., Neville A. and Taylor J. D. "An Assessment of the Formation of Electrodeposited Scales Using Scanning Electron and Atomic Microscopy", Journal of Crystal Growth, Vol. 237, pp. 2160-2165 (2002).

[13] Gabe D. R., Wilcox G. D., Garcia J. G. and Walsh F. C. " The Rotating Cylinder Electrode: its continued development and application", Journal of Applied Electrochemistry, Vol. 28, pp. 759-780 (1998).

[14] Branch C. A. and Muller-Steinhagen H. "Influence of Scaling on the Performance of Shell-and-Tube Heat Exchangers." Heat Transfer Engineering, Vol. 12, Issue no. 2, pp. 37-45 (1991).

[15] Fahiminia F., Paul Watkinson A. and Epstin N. "Investigation of Initial Fouling Rates of Calcium Sulfate Solution Under Non-boiling Conditions." Engineering Conferences International Symposium Series, Vol. RPI, article 5 (2003).

[16] Sheikhholeslami R. and Ng M. "Calcium Sulfate Precipitation in the Presence of Nondominant Calcium Carbonate: Thermodynamics and Kinetics." Ind. Eng. Chem. Res., Vol. 40, pp. 3570-3578 (2001).

[17] Behbahani R. M., Muller-Steinhagen H. and Jamialahmadi M. "Investigation of Scale Formation in Heat Exchangers of Phosphoric Acis Evaporaters Plants." the Canadian Journal of Chemical Engineering, Vol. 84, pp. 189-197 April (2006).

[18] Helalizadeh, Steinhagen M. and Jamialahmadi M. "Crystallization Fouling of Mixed Salts During Convective Heat Transfer and Sub-Cooled Flow Boiling Conditions." Engineering Conferences International Symposium Series, Vol. RPI, article 6 (2003).

[19] Yang Q., Liu Y., Gu A., Ding J., Shen Z. "Investigation of Induction Period and Morphology of $CaCO_3$ Fouling on Heated Surface" Chemical Engineering Science, Vol. 57, pp. 921-931 (2002).

[20] Klaren D. G., Boer E. F. and W D. "Zero Fouling Self Cleaning Heat Exchanger" Heat Transfer Engineering, Vol. 28(3), pp. 216-221 (2007).

[21] Liu G., Tree D. A., and High M. S. "Relationship Between Rotating Disc Corrosion Measurment and Corrosion in Pipe Flow" The Journal of Science and Engineering Corrosion, NACE, Vol. 50, pp. 584-593 (1994).

[22] Efrid K. D., Wright E. J., Boros J. A. and Hailey T. G. The Journal of Science and Engineering Corrosion, NACE, Vol. 49, pp. 992-1003 (1993).

[23] Silverman D.C. “Rotating Cylinder Electrode for Velocity Sensitivity Testing”, Corrosion, Vol. 40, No. 5, pp.220-226 (1984).

[24] Ashiru O. A. and Farr J. P. Journal of Electrochemistry Society, Vol. 139, pp.2806-2810 (1992).

[25] Khokhar M. I., Quddus A., Allam I. M. and Abbasi T. A. Proceeding, 6th Middle East Corrosion Conference, Bahrain, Vol. 2, pp.759-769 (1994).

[26] Neville A., Morizot A. P Hodgkiess T. "Electrochemical aspects of surface/solution interactions in scale initiation and growth", Vol. 37, No. 5, pp. 50-57 Material Performance, (May 1998).

[27] Levich V. G., "Physicochemical Hydrodynamics", Prentice-Hall, Englewood Cliffs, NJ, (1962).

[28] Coleman, H. W. and Steele, W. G. “Experimental and Uncertainty Analysis for Engineers,” Wiley, New York, (1999).

[29] Taylor B.N. and Kuyatt C. E. “Guidelines for Evaluating and Expressing the Uncertainty of NIST Measurement Results”, *National Institute of Standards and Technology* Technical Note 1297, (1994).

[30] Figliola R. S., and Beasely, D. E. “Theory and Design of Mechanical measurements”, 3rd Edition, Wiley Publishing house, (2000).

Vita

Abdullah A. Al-Mesfer

Born in Khobar, Saudi Arabia in 1975

Received Bachelor's degree in Mechanical Engineering from King Fahd University of Petroleum and Minerals (KFUPM), Dhahran, Saudi Arabia in 1999.

Currently working in Saudi Aramco with Consulting Services Department as Energy Engineer.

Completed Master's degree in Mechanical Engineering at KFUPM, May 2008.

APPENDICES

APPENDIX A

SAMPLE CALCULATIONS OF DEPOSITION RATE AND REYNOLDS NUMBER

In APPENDIX A we present all the calculations for deposition rate experiments conducted during the present study. Also, the complete calculation of the uncertainty analysis for all values is presented

A.1 Sample of Deposition Rate Calculation

The following sets of tables (Tables A1-A8) are related to the number of measurements taken for deposition rate during our experimental work.

Table A.1: Set-I of Scale Deposition Rates for 120-G Aluminum Samples

Sr. #	Speed (rpm)	Equivalent Re	Log_{10} (Re)	D_r ($g\ m^{-2}\ h^{-1}$)	log_{10} (D_r)
1	50	746	2.873	11.625	1.012
2	100	1492	3.174	15.215	1.088
3	250	3730	3.572	22.455	1.320
4	500	7460	3.873	36.064	1.494
5	750	11190	4.049	38.927	1.628
6	1000	14921	4.174	55.925	1.790
7	1250	18651	4.271	70.746	1.886
8	1500	22381	4.350	75.668	1.914
9	1750	26111	4.417	81.738	1.917
10	2000	29841	4.475	83.893	1.925

Table A.2: Set-II of Scale Deposition Rates for 120-G Aluminum Samples

Sr. #	Speed (rpm)	Equivalent Re	Log_{10} (Re)	D_r ($g\ m^{-2}\ h^{-1}$)	log_{10} (D_r)
1	50	746	2.873	10.045	1.012
2	100	1492	3.174	13.766	1.088
3	250	3730	3.572	21.209	1.320
4	500	7460	3.873	30.857	1.494
5	750	11190	4.049	45.872	1.628
6	1000	14921	4.174	58.992	1.790
7	1250	18651	4.271	79.348	1.886
8	1500	22381	4.350	82.296	1.914
9	1750	26111	4.417	80.639	1.917
10	2000	29841	4.475	84.75	1.925

Table A.3: Set-III of Scale Deposition Rates for 120-G Aluminum Samples

Sr. #	Speed (rpm)	Equivalent Re	Log_{10} (Re)	D_r (g m^{-2} h^{-1})	log_{10} (D_r)
1	50	746	2.873	9.203	1.012
2	100	1492	3.174	7.763	1.088
3	250	3730	3.572	19.066	1.320
4	500	7460	3.873	26.583	1.494
5	750	11190	4.049	42.731	1.628
6	1000	14921	4.174	70.117	1.790
7	1250	18651	4.271	80.804	1.886
8	1500	22381	4.350	88.024	1.914
9	1750	26111	4.417	85.351	1.917
10	2000	29841	4.475	83.786	1.925

Table A.4: Average Scale Deposition Rates for 120-G Aluminum Samples

Sr. #	Equivalent Re	D_{r1} ($g\ m^{-2}\ h^{-1}$)	D_{r2} ($g\ m^{-2}\ h^{-1}$)	D_{r3} ($g\ m^{-2}\ h^{-1}$)	$D_{r\text{-}avg}$ ($g\ m^{-2}\ h^{-1}$)
1	746	11.625	10.045	9.203	10.291
2	1492	15.215	13.766	7.763	12.248
3	3730	22.455	21.209	19.066	20.910
4	7460	36.064	30.857	26.583	31.168
5	11190	38.927	45.872	42.731	42.510
6	14921	55.925	58.992	70.117	61.678
7	18651	70.746	79.348	80.804	76.966
8	22381	75.668	82.296	88.024	81.996
9	26111	81.738	80.639	85.351	82.576
10	29841	83.893	84.75	83.786	84.143

Table A.5: Set-I of Scale Deposition Rates for 600-G Aluminum Samples

Sr. #	Speed (rpm)	Equivalent Re	Log_{10} (Re)	D_r ($g\ m^{-2}\ h^{-1}$)	log_{10} (D_r)
1	50	746	2.873	4.432	0.6812
2	100	1492	3.174	7.505	0.9434
3	250	3730	3.572	13.611	1.0653
4	500	7460	3.873	20.569	1.3742
5	750	11190	4.049	42.159	1.5993
6	1000	14921	4.174	52.169	1.7496
7	1250	18651	4.271	60.634	1.7654
8	1500	22381	4.350	59.856	1.7705
9	1750	26111	4.417	59.57	1.777
10	2000	29841	4.475	61.231	1.7819

Table A.6: Set-II of Scale Deposition Rate for 600-G Aluminum Samples

Sr. #	Speed (rpm)	Equivalent Re	Log_{10} (Re)	D_r ($g\ m^{-2}\ h^{-1}$)	log_{10} (D_r)
1	50	746	2.873	5.678	0.6812
2	100	1492	3.174	9.587	0.9434
3	250	3730	3.572	10.734	1.0653
4	500	7460	3.873	24.297	1.3742
5	750	11190	4.049	38.776	1.5993
6	1000	14921	4.174	61.505	1.7496
7	1250	18651	4.271	57.439	1.7654
8	1500	22381	4.350	60.122	1.7705
9	1750	26111	4.417	59.224	1.777
10	2000	29841	4.475	59.958	1.7819

Table A.7: Set-III of Scale Deposition Rate for 600-G Aluminum Samples

Sr. #	Speed (rpm)	Equivalent Re	Log_{10} (Re)	D_r ($g\ m^{-2}\ h^{-1}$)	log_{10} (D_r)
1	50	746	2.873	4.29	0.6812
2	100	1492	3.174	9.242	0.9434
3	250	3730	3.572	10.521	1.0653
4	500	7460	3.873	26.15	1.3742
5	750	11190	4.049	38.312	1.5993
6	1000	14921	4.174	54.887	1.7496
7	1250	18651	4.271	56.704	1.7654
8	1500	22381	4.350	56.869	1.7705
9	1750	26111	4.417	60.717	1.777
10	2000	29841	4.475	60.392	1.7819

Table A.8: Average Scale Deposition Rate for 600-G Aluminum Samples

Sr. #	Equivalent Re	D_{r1} (g m^{-2} h^{-1})	D_{r2} (g m^{-2} h^{-1})	D_{r3} (g m^{-2} h^{-1})	$D_{r\text{-}avg}$ (g m^{-2} h^{-1})
1	746	4.432	5.678	4.29	4.800
2	1492	7.505	9.587	9.242	8.778
3	3730	13.611	10.734	10.521	11.622
4	7460	20.569	24.297	26.15	23.672
5	11190	42.159	38.776	38.312	39.749
6	14921	52.169	61.505	54.887	56.187
7	18651	60.634	57.439	56.704	58.259
8	22381	59.856	60.122	56.869	58.949
9	26111	59.57	59.224	60.717	59.837
10	29841	61.231	59.958	60.392	60.527

A.2 Uncertainty for Deposition rates and Reynolds Numbers

In this section we show the uncertainty calculation for all the measured deposition rates for 120-G and 600-G samples respectively [Tables A9-A18 and A20-A29], followed by the uncertainty calculation of all Reynolds numbers [Tables A31-A40]. For each calculation, a separate respective table is shown containing summary of all results [Table A19, A30 and A41].

Table A.9: Uncertainty Calculation for Measured D_r = 10.291 at Re= 746 (120-G)

Variable Uncertainty	Partial Derivative	% of Sensitivity
D_r= 10.291 ± 0.3073		
D = 0.0127 ± 0.00025	$\partial Dr / \partial D =$ -810.6	43.49 %
L = 0.0127 ± 0.0002	$\partial Dr / \partial L =$ -810.6	27.84 %
T = 6 ± 0.003	$\partial Dr / \partial T =$ -1.716	0.03 %
W_g = 0.0313 ± 0.0005	$\partial Dr / \partial W =$ 328.9	28.64 %

Table A.10: Uncertainty Calculation for Measured D_r = 12.248 at Re= 1492 (120-G)

Variable Uncertainty	Partial Derivative	% of Uncertainty
D_r=12.248 ± 0.3503		
D = 0.0127 ± 0.00025	$\partial Dr / \partial D =$ -966	47.52 %
L = 0.0127 ± 0.0002	$\partial Dr / \partial L =$ -966	30.41 %
T = 6 ± 0.003	$\partial Dr / \partial T =$ -2.045	0.03 %
W_g = 0.0373 ± 0.0005	$\partial Dr / \partial W =$ 328.9	22.04 %

Table A.11: Uncertainty Calculation for Measured D_r = 20.910 at Re= 3730 (120-G)

Variable Uncertainty	Partial Derivative	% of Uncertainty
D_r= 20.910 ± 0.5525		
D = 0.0127 ± 0.00025	$\partial Dr / \partial D =$ -1647	55.55 %
L = 0.0127 ± 0.0002	$\partial Dr / \partial L =$ -1647	35.55 %
T = 6 ± 0.003	$\partial Dr / \partial T =$ -3.487	0.04 %
W_g = 0.0636 ± 0.0005	$\partial Dr / \partial W =$ 328.9	8.86 %

Table A.12: Uncertainty Calculation for Measured D_r = 31.168 at Re= 7460 (120-G)

Variable Uncertainty	Partial Derivative	% of Uncertainty
D_r= 31.168 ± 0.8032		
D = 0.0127 ± 0.00025	$\partial Dr / \partial D =$ -2455	58.40 %
L = 0.0127 ± 0.0002	$\partial Dr / \partial L =$ -2455	37.37 %
T = 6 ± 0.003	$\partial Dr / \partial T =$ -5.197	0.04 %
W_g = 0.0948 ± 0.0005	$\partial Dr / \partial W =$ 328.9	4.19 %

Table A.13: Uncertainty Calculation for Measured D_r = 42.510 at Re= 11190 (120-G)

Variable Uncertainty	Partial Derivative	% of Uncertainty
D_r= 42.510 ± 1.085		
D = 0.0127 ± 0.00025	$\partial Dr / \partial D =$ -3349	59.55 %
L = 0.0127 ± 0.0002	$\partial Dr / \partial L =$ -3349	38.11 %
T = 6 ± 0.003	$\partial Dr / \partial T =$ -7.088	0.04 %
W_g = 0.1293 ± 0.0005	$\partial Dr / \partial W =$ 328.9	2.30 %

Table A.14: Uncertainty Calculation for Measured D_r = 61.678 at Re= 14921 (120-G)

Variable Uncertainty	Partial Derivative	% of Uncertainty
D_r= 61.678 ± 1.085		
D = 0.0127 ± 0.00025	$\partial Dr / \partial D =$ -4859	60.28 %
L = 0.0127 ± 0.0002	$\partial Dr / \partial L =$ -4859	38.58 %
T = 6 ± 0.003	$\partial Dr / \partial T =$ -10.28	0.04 %
W_g = 0.1876 ± 0.0005	$\partial Dr / \partial W =$ 328.9	1.10 %

Table A.15: Uncertainty Calculation for Measured D_r = 76.966 at Re= 18651 (120-G)

Variable Uncertainty	Partial Derivative	% of Uncertainty
D_r= 76.966 ± 1.948		
D = 0.0127 ± 0.00025	$\partial Dr / \partial D =$ -6063	60.52 %
L = 0.0127 ± 0.0002	$\partial Dr / \partial L =$ -6063	38.73 %
T = 6 ± 0.003	$\partial Dr / \partial T =$ -12.83	0.04 %
W_g = 0.2341 ± 0.0005	$\partial Dr / \partial W =$ 328.9	0.71 %

Table A.16: Uncertainty Calculation for Measured D_r = 81.966 at Re= 22381 (120-G)

Variable Uncertainty	Partial Derivative	% of Uncertainty
D_r= 81.996 ± 2.075		
D = 0.0127 ± 0.00025	$\partial Dr / \partial D =$ -6459	60.57 %
L = 0.0127 ± 0.0002	$\partial Dr / \partial L =$ -6459	38.76 %
T = 6 ± 0.003	$\partial Dr / \partial T =$ -13.67	0.04 %
W_g = 0.2494 ± 0.0005	$\partial Dr / \partial W =$ 328.9	0.62 %

Table A.17: Uncertainty Calculation for Measured D_r = 82.576 at Re= 26111 (120-G)

Variable Uncertainty	Partial Derivative	% of Uncertainty
D_r= 82.576 ± 2.090		
D = 0.0127 ± 0.00025	D = 0.0127 ± 0.00025	D = 0.0127 ± 0.00025
L = 0.0127 ± 0.0002	L = 0.0127 ± 0.0002	L = 0.0127 ± 0.0002
T = 6 ± 0.003	T = 6 ± 0.003	T = 6 ± 0.003
W_g = 0.2512 ± 0.0005	W_g = 0.2512 ± 0.0005	W_g = 0.2512 ± 0.0005

Table A.18: Uncertainty Calculation for Measured D_r = 84.143 at Re= 29841 (120-G)

Variable Uncertainty	Partial Derivative	% of Uncertainty
D_r= 84.143 ± 2.129		
D = 0.0127 ± 0.00025	D = 0.0127 ± 0.00025	D = 0.0127 ± 0.00025
L = 0.0127 ± 0.0002	L = 0.0127 ± 0.0002	L = 0.0127 ± 0.0002
T = 6 ± 0.003	T = 6 ± 0.003	T = 6 ± 0.003
W_g = 0.2559 ± 0.0005	W_g = 0.2559 ± 0.0005	W_g = 0.2559 ± 0.0005

Table A.19: Summary of Uncertainty Calculation for 120-G Samples

Sr. #	Speed (rpm)	Re	D_r ($g\ m^{-2}\ h^{-1}$)	% Uncertainty
1	50	746	10.291	2.99
2	100	1492	12.248	2.86
3	250	3730	20.91	2.64
4	500	7460	31.168	2.58
5	750	11190	42.51	2.55
6	1000	14921	61.678	2.12
7	1250	18651	76.966	2.53
8	1500	22381	81.996	2.53
9	1750	26111	82.576	2.53
10	2000	29841	84.143	2.53

Table A.20: Uncertainty Calculation for Measured D_r = 4.800 at Re= 746 (600-G)

Variable Uncertainty	Partial Derivative	% of Uncertainty
D_r=4.800 ± 0.2042		
D = 0.0127 ± 0.0002	$\partial Dr / \partial D =$ -378.1	21.43 %
L = 0.0127 ± 0.0002	$\partial Dr / \partial L =$ -378.1	13.71 %
T = 6 ± 0.003	$\partial Dr / \partial T =$ -0.8004	0.01 %
W_g = 0.0146 ± 0.0005	$\partial Dr / \partial W =$ 328.9	64.85 %

Table A.21: Uncertainty Calculation for Measured D_r = 8.778 at Re= 1492 (600-G)

Variable Uncertainty	Partial Derivative	% of Uncertainty
D_r=8.778 ± 0.2758		
D = 0.0127 ± 0.00025	$\partial Dr / \partial D =$ -691.5	39.28 %
L = 0.0127 ± 0.0002	$\partial Dr / \partial L =$ -691.5	25.14 %
T = 6 ± 0.003	$\partial Dr / \partial T =$ -1.464	0.03 %
W_g = 0.0267 ± 0.0005	$\partial Dr / \partial W =$ 328.9	35.55 %

Table A.22: Uncertainty Calculation for Measured D_r = 11.622 at Re= 3730 (600-G)

Variable Uncertainty	Partial Derivative	% of Uncertainty
D_r=11.622 ± 0.3358		
D = 0.0127 ± 0.00025	$\partial Dr / \partial D =$ -914.2	46.33 %
L = 0.0127 ± 0.0002	$\partial Dr / \partial L =$ -914.2	29.65 %
T = 6 ± 0.003	$\partial Dr / \partial T =$ -0.01	0.03 %
W_g = 0.0353 ± 0.0005	$\partial Dr / \partial W =$ 328.9	23.99 %

Table A.23: Uncertainty Calculation for Measured D_r = 23.672 at Re= 7460 (600-G)

Variable Uncertainty	Partial Derivative	% of Uncertainty
D_r=23.672 ± 0.6194		
D = 0.0127 ± 0.00025	$\partial Dr / \partial D =$ -1865	56.65 %
L = 0.0127 ± 0.0002	$\partial Dr / \partial L =$ -1865	36.25 %
T = 6 ± 0.003	$\partial Dr / \partial T =$ -3.947	0.04 %
W_g = 0.0720 ± 0.0005	$\partial Dr / \partial W =$ 328.9	7.05 %

Table A.24: Uncertainty Calculation for Measured D_r = 39.749 at Re= 11190 (600-G)

Variable Uncertainty	Partial Derivative	% of Uncertainty
D_r= 39.749 ± 1.016		
D = 0.0127 ± 0.00025	$\partial Dr / \partial D =$ -3131	59.35 %
L = 0.0127 ± 0.0002	$\partial Dr / \partial L =$ -3131	37.99 %
T = 6 ± 0.003	$\partial Dr / \partial T =$ -6.629	0.04 %
W_g = 0.1209 ± 0.0005	$\partial Dr / \partial W =$ 328.9	2.62 %

Table A.25: Uncertainty Calculation for Measured D_r = 56.187 at Re= 14921 (600-G)

Variable Uncertainty	Partial Derivative	% of Uncertainty
D_r= 56.187 ± 1.427		
D = 0.0127 ± 0.00025	$\partial Dr / \partial D =$ -4426	60.14 %
L = 0.0127 ± 0.0002	$\partial Dr / \partial L =$ -4426	38.49 %
T = 6 ± 0.003	$\partial Dr / \partial T =$ -9.369	0.04 %
W_g = 0.1709 ± 0.0005	$\partial Dr / \partial W =$ 328.9	1.33 %

Table A.26: Uncertainty Calculation for Measured D_r = 58.259 at Re= 18651 (600-G)

Variable Uncertainty	Partial Derivative	% of Uncertainty
D_r= 58.259 ± 1.479		
D = 0.0127 ± 0.00025	D = 0.0127 ± 0.00025	D = 0.0127 ± 0.00025
L = 0.0127 ± 0.0002	L = 0.0127 ± 0.0002	L = 0.0127 ± 0.0002
T = 6 ± 0.003	T = 6 ± 0.003	T = 6 ± 0.003
W_g = 0.1772 ± 0.0005	W_g = 0.1772 ± 0.0005	W_g = 0.1772 ± 0.0005

Table A.27: Uncertainty Calculation for Measured D_r = 58.949 at Re= 22381 (600-G)

Variable Uncertainty	Partial Derivative	% of Uncertainty
D_r= 58.949 ± 1.496		
D = 0.0127 ± 0.00025	$\partial Dr / \partial D =$ -4644	60.22 %
L = 0.0127 ± 0.0002	$\partial Dr / \partial L =$ -4644	38.54 %
T = 6 ± 0.003	$\partial Dr / \partial T =$ -9.829	0.04 %
W_g = 0.1793 ± 0.0005	$\partial Dr / \partial W =$ 328.9	1.21 %

Table A.28: Uncertainty Calculation for Measured D_r = 59.837 at Re= 26111 (600-G)

Variable Uncertainty	Partial Derivative	% of Uncertainty
D_r= 59.837 ± 1.518		
D = 0.0127 ± 0.00025	D = 0.0127 ± 0.00025	D = 0.0127 ± 0.00025
L = 0.0127 ± 0.0002	L = 0.0127 ± 0.0002	L = 0.0127 ± 0.0002
T = 6 ± 0.003	T = 6 ± 0.003	T = 6 ± 0.003
W_g = 0.1820 ± 0.0005	W_g = 0.1820 ± 0.0005	W_g = 0.1820 ± 0.0005

Table A.29: Uncertainty Calculation for Measured D_r = 60.527 at Re= 29841 (600-G)

Variable Uncertainty	Partial Derivative	% of Uncertainty
D_r= 60.527 ± 1.536		
D = 0.0127 ± 0.00025	D = 0.0127 ± 0.00025	D = 0.0127 ± 0.00025
L = 0.0127 ± 0.0002	L = 0.0127 ± 0.0002	L = 0.0127 ± 0.0002
T = 6 ± 0.003	T = 6 ± 0.003	T = 6 ± 0.003
W_g = 0.1841 ± 0.0005	W_g = 0.1841 ± 0.0005	W_g = 0.1841 ± 0.0005

Table A.30: Summary of Uncertainty Calculation for 600-G Samples

Sr. #	Speed (rpm)	Re	D_r ($g\ m^{-2}\ h^{-1}$)	% Uncertainty
1	50	746	4.800	4.25
2	100	1492	8.778	3.14
3	250	3730	11.622	2.89
4	500	7460	23.672	2.62
5	750	11190	39.749	2.56
6	1000	14921	56.187	2.54
7	1250	18651	58.259	2.54
8	1500	22381	58.949	2.54
9	1750	26111	59.837	2.54
10	2000	29841	60.527	2.54

Table A.31: Uncertainty Calculation for Reynolds Number (Re) = 746

Variable Uncertainty	Partial Derivative	% of Uncertainty
Re=746 ±16.83		
R_1 = 0.0127 ±0.00025	$\partial \mathrm{Re}/\partial R_1 = 23710$	12.40 %
R_2 = 0.034 ±0.00025	$\partial \mathrm{Re}/\partial R_2 = 35014$	27.04 %
ν = 0.000001897 ±3.000E-08	$\partial \mathrm{Re}/\partial \nu =$ -3.931 E+08	49.08 %
ω = 5.23 ±0.04	$\partial \mathrm{Re}/\partial \omega = 142.6$	11.48 %

Table A.32: Uncertainty Calculation for Reynolds Number (Re) = 1492

Variable Uncertainty	Partial Derivative	% of Uncertainty
Re=1492 ±32.19		
R_1 = 0.0127 ±0.00025	$\partial \mathrm{Re}/\partial R_1 = 47420$	13.57 %
R_2 = 0.034 ±0.00025	$\partial \mathrm{Re}/\partial R_2 = 70027$	29.58 %
ν = 0.000001897 ±3.000E-08	$\partial \mathrm{Re}/\partial \nu =$ -7.864 E+08	53.71 %
ω = 10.46 ±0.04	$\partial \mathrm{Re}/\partial \omega = 142.6$	3.14 %

Table A.33: Uncertainty Calculation for Reynolds Number (Re) = 3730

Variable Uncertainty	Partial Derivative	% of Uncertainty
Re=3730 ± 79.40		
R_1 = 0.0127 ±0.00025	$\partial \mathrm{Re}/\partial R_1 = 118550$	13.93 %
R_2 = 0.034 ±0.00025	$\partial \mathrm{Re}/\partial R_2 = 175069$	30.39 %
ν = 0.000001897 ±3.000E-08	$\partial \mathrm{Re}/\partial \nu$ = -1.966 E+09	55.16 %
ω = 52.3 ±0.04	$\partial \mathrm{Re}/\partial \omega = 142.6$	0.52 %

Table A.34: Uncertainty Calculation for Reynolds Number (Re) = 7460

Variable Uncertainty	Partial Derivative	% of Uncertainty
Re=7460 ± 158.5		
R_1 = 0.0127 ±0.00025	$\partial \mathrm{Re}/\partial R_1 = 237101$	13.99 %
R_2 = 0.034 ±0.00025	$\partial \mathrm{Re}/\partial R_2 = 350137$	30.50 %
ν = 0.000001897 ±3.000E-08	$\partial \mathrm{Re}/\partial \nu =$ -3.93 E+09	55.38 %
ω = 52.3 ±0.04	$\partial \mathrm{Re}/\partial \omega = 142.6$	0.13 %

Table A.35: Uncertainty Calculation for Reynolds Number (Re) = 11190

Variable Uncertainty	Partial Derivative	% of Uncertainty
Re=11190 ± 237.6		
R_1 = 0.0127 ±0.00025	R_1 = 0.0127 ±0.00025	R_1 = 0.0127 ±0.00025
R_2 = 0.034 ±0.00025	R_2 = 0.034 ±0.00025	R_2 = 0.034 ±0.00025
ν = 0.000001897 ±3.000E-08	ν = 0.000001897 ±3.000E-08	ν = 0.000001897
ω = 78.45 ± 0.04	ω = 78.45 ± 0.04	ω = 78.45 ± 0.04

Table A.36: Uncertainty Calculation for Reynolds Number (Re) = 14921

Variable Uncertainty	Partial Derivative	% of Uncertainty
Re=14921 ± 316.8		
R_1 = 0.0127 ±0.00025	R_1 = 0.0127 ±0.00025	R_1 = 0.0127 ±0.00025
R_2 = 0.034 ±0.00025	R_2 = 0.034 ±0.00025	R_2 = 0.034 ±0.00025
ν = 0.000001897 ±3.000E-08	ν = 0.000001897 ±3.000E-08	ν = 0.000001897
ω = 104.6 ± 0.04	ω = 104.6 ± 0.04	ω = 104.6 ± 0.04

Table A.37: Uncertainty Calculation for Reynolds Number (Re) = 18651

Variable Uncertainty	Partial Derivative	% of Uncertainty
Re= 18651 ± 396		
R_1 = 0.0127 ±0.00025	$\partial \mathrm{Re}/\partial R_1 = 592752$	14 %
R_2 = 0.034 ±0.00025	$\partial \mathrm{Re}/\partial R_2 = 875343$	30.54 %
ν = 0.000001897 ±3.000E-08	$\partial \mathrm{Re}/\partial \nu =$ -9.829 E+09	55.44 %
ω = 130.8 ±0.04	$\partial \mathrm{Re}/\partial \omega = 142.6$	0.02 %

Table A.38: Uncertainty Calculation for Reynolds Number (Re) = 22381

Variable Uncertainty	Partial Derivative	% of Uncertainty
Re= 22381 ± 465		
R_1 = 0.0127 ±0.00025	R_1 = 0.0127 ±0.00025	R_1 = 0.0127 ±0.00025
R_2 = 0.034 ±0.00025	R_2 = 0.034 ±0.00025	R_2 = 0.034 ±0.00025
ν = 0.000001897 ±3.000E-08	ν = 0.000001897 ±3.000E-08	ν = 0.000001897
ω = 156.9 ± 0.04	ω = 156.9 ± 0.04	ω = 156.9 ± 0.04

Table A.39: Uncertainty Calculation for Reynolds Number (Re) = 26111

Variable Uncertainty	Partial Derivative	% of Uncertainty
Re= 26111 ± 537		
R_1 = 0.0127 ±0.00025	R_1 = 0.0127 ±0.00025	R_1 = 0.0127 ±0.00025
R_2 = 0.034 ±0.00025	R_2 = 0.034 ±0.00025	R_2 = 0.034 ±0.00025
ν = 0.000001897 ±3.000E-08	ν = 0.000001897 ±3.000E-08	ν = 0.000001897
ω = 183.1 ± 0.04	ω = 183.1 ± 0.04	ω = 183.1 ± 0.04

Table A.40: Uncertainty Calculation for Reynolds Number (Re) = 29841

Variable Uncertainty	Partial Derivative	% of Uncertainty
Re=29841 ± 603		
R_1 = 0.0127 ±0.00025	$\partial \mathrm{Re}/\partial R_1 = 948403$	14 %
R_2 = 0.034 ±0.00025	$\partial \mathrm{Re}/\partial R_2 = 1.401$ E +10	30.54 %
ν = 0.000001897 ±3.000E-08	$\partial \mathrm{Re}/\partial \nu =$ -1.572 E+10	55.45 %
ω = 209.2 ±0.04	$\partial \mathrm{Re}/\partial \omega = 142.6$	0.01 %

Table A.41: Summary of Uncertainty Calculation for Reynolds Number

Sr. #	Speed (rpm)	Re	% Uncertainty
1	50	746	2.26
2	100	1492	2.16
3	250	3730	2.13
4	500	7460	2.12
5	750	11190	2.12
6	1000	14921	2.12
7	1250	18651	2.12
8	1500	22381	2.08
9	1750	26111	2.06
10	2000	29841	2.02